



## JAMES | Journal of Advances in Modeling Earth Systems\*



#### RESEARCH ARTICLE

10.1029/2021MS002863

#### **Key Points:**

- Global surface ocean eddy heat fluxes (EHFs) are reconstructed from 1993 to 2017 based on satellite observations
- The divergent component is successfully extracted on the globe by performing a Helmholtz decomposition
- EHF and its associated energy conversion rates in a high-resolution coupled model agree well with observation-based estimates

#### Correspondence to:

Y. Guo, yguo20@ncsu.edu

#### Citation:

Guo, Y., & Bishop, S. P. (2022). Surface divergent eddy heat fluxes and their impacts on mixed layer eddymean flow interactions. *Journal of Advances in Modeling Earth Systems*, 14, e2021MS002863. https://doi.org/10.1029/2021MS002863

Received 6 OCT 2021 Accepted 1 APR 2022

© 2022 The Authors. Journal of Advances in Modeling Earth Systems published by Wiley Periodicals LLC on behalf of American Geophysical Union. This is an open access article under the terms of the Creative Commons Attribution License, which permits use, distribution and reproduction in any medium, provided the original work is properly cited.

# **Surface Divergent Eddy Heat Fluxes and Their Impacts on Mixed Layer Eddy-Mean Flow Interactions**

Yiming Guo<sup>1</sup> and Stuart P. Bishop<sup>1</sup>

<sup>1</sup>North Carolina State University, Raleigh, NC, USA

**Abstract** In this study, the global surface divergent eddy heat flux (EHF) is estimated using remote sensing observations of sea surface height (SSH) and sea surface temperature (SST) over two decades (1993–2017). These results are used as a metric to assess model fidelity in a mesoscale eddy-resolving version of the Community Earth System Model. The estimated EHFs show that the midlatitudes significantly contribute to the poleward transport of heat because of strong regional variability in SSH and SST. A Helmholtz decomposition is performed on the global EHFs to remove prominent nondynamic rotational wave-like structures that appear in these fluxes. The dynamic divergent EHFs are responsible for driving cross-frontal exchange and positive Baroclinic Conversion (BC) rates, suggesting a conversion of mean potential energy to eddy potential energy within the mixed layer. The results show that the model captures the same spatial patterns of EHFs and BC rates, but with relatively higher values in the midlatitudes than observations. The mixed layer geostrophic meridional eddy heat transport reaches maximums of 0.07 PW and 0.1 PW in the midlatitudes in the observations and climate model, respectively. The global integrated BC rate is 0.11 TW in the observations, which is ~30% weaker than the climate model (0.16 TW). A cross-spectral analysis further shows that the model has higher energy in low-frequency bands for periods greater than 10 months in the northern hemisphere western boundary currents, but can capture the major spectral peaks in EHFs that are seen in observations.

**Plain Language Summary** Mesoscale eddies are ubiquitous in the ocean and play a pivotal role in the transport of heat. Previous study showed that eddies explain about 1/3 of variation of total heat transport in the ocean. In this work, we reconstructed the long-term global ocean surface heat transport by mesoscale eddies for the first time by using satellite observations. In addition, the eddy heat transport was further decomposed into rotational and divergent fields, where only the divergent part plays the actual dynamic role in poleward transport of heat. From our estimates of divergent eddy heat transport, we are additionally able to quantify how the potential energy transfers between large-scale ocean currents and small-scale eddies in the ocean surface. Comparison between observation-based results and a high-resolution climate model show good performance of the model to capture the signal of eddy heat fluxes, however, larger variability is found in the model.

#### 1. Introduction

Mesoscale eddies, characterized by spatial scales from tens to hundreds of kilometers and temporal scales from tens to hundreds of days, are thought to be one of the largest contributions to ocean variability and tracer transport (Chelton, Gaube, et al., 2011; Chelton, Schlax, & Samelson, 2011; Stammer, 1998). Mesoscale eddy heat transport has been found to play a key role in the global heat balance (Dong et al., 2014; Volkov et al., 2008). However, insufficient observations throughout the water column at the needed time and space scales have made it challenging to determine their global contribution to heat transport; with most studies being primarily model-based (Aoki et al., 2013; Jayne & Marotzke, 2002; Volkov et al., 2008). Regional studies have focused on eddy heat flux (EHF) and transport using in situ observations in the Kuroshio Extension (Bishop, 2013; Bishop et al., 2013), the Gulf Stream (M. Cronin & Watts, 1996; Dewar & Bane, 1989; Hall, 1986), and the Southern Ocean (Phillips & Rintoul, 2000; Watts et al., 2016), but these studies were relatively short in duration with one- to two-year time series in a limited spatial domain.

In recent years, remotely sensed observations of the sea surface height (SSH) and sea surface temperature (SST) have been utilized in unique ways to estimate surface EHF and transport. By using in situ measurements in Drake Passage combined with satellite SSH data, Foppert et al. (2017) defined a circumpolar EHF proxy based on SSH standard deviation through a power law that was determined from the eddy-permitting Southern Ocean State Estimate. Abernathey and Wortham (2015) quantified the wavenumber-frequency spectrum of surface EHFs and

GUO AND BISHOP 1 of 19



zonally integrated mixed-layer eddy heat transport in a swath of the Eastern Pacific using satellite observations and a high-resolution coupled climate model. Their study, however, was limited to an area of the ocean where mesoscale eddy kinetic energy is much weaker than in the western boundary currents. In this study, we will extend their analysis to global, including the energetic western boundary currents.

In order to properly interpret EHFs, it is necessary to perform a Helmholtz decomposition of the fluxes into divergent and rotational components. Marshall and Shutts (1981) demonstrate a dynamically based understanding of the Helmholtz decomposition for EHFs using the temperature variance equation, as a proxy for eddy potential energy (EPE) equation. Their results show that the divergent EHFs balance the conversion of EPE to eddy kinetic energy in the baroclinic instability, and the rotational EHFs are only associated with the spatial growth and decay of eddies and is balanced by the mean advection of EPE. It is shown that the rotational EHF field accounts for large eddy diffusivities with a fluctuating sign along mean isopycnal surfaces, which impacts both the eddy-induced tracer advection and diffusion (Eden et al., 2007; Zhai & Greatbatch, 2006). For a local analysis of energetics, it is necessary to remove the large and nondynamic rotational EHFs. However, the Helmholtz decomposition comes with its own set of challenges when choosing appropriate boundary conditions, which have been postulated to be indeterminate (Fox-Kemper et al., 2003). A regional decomposition was performed in the Kuroshio Extension (Bishop et al., 2013) and Gulf Stream (M. Cronin & Watts, 1996; Zhai & Greatbatch, 2006) by assuming the rotational flux is linearly proportional to the gradient of temperature variance when the mean flow is approximately equivalent barotropic (Marshall & Shutts, 1981). However, this method cannot guarantee a fully two-dimensional non-divergent rotational flux (Zhai & Greatbatch, 2006) and the corresponding divergent flux may contain a nontrivial rotational component (Bishop et al., 2013). Alternatively, the rotational EHF can be removed through a Helmholtz decomposition by solving the 2D Poisson equation globally (see details in Section 2). This decomposition has been applied previously to the depth-integrated EHFs in Jayne and Marotzke (2002), Aoki et al. (2013), and Abernathey and Cessi (2014). Here, we update this work by performing a Helmholtz decomposition using 25 years of global surface observations and a high-resolution climate model with a computationally efficient method for solving the Poisson equation on a global grid. This will allow us to further uncover the spatiotemporal variability in the divergent EHFs and access their contributions to ocean energetics.

Traditional ocean components in climate models do not directly resolve mesoscale and smaller ocean processes, which are parameterized with different dynamically based schemes, for example, Gent and Mcwilliams (1990) (hereafter referred to as GM). The goal of the GM parametrization is to represent the unresolved divergent EHFs by a flux-gradient relationship. Recent improvements on climate simulations have shown that the ocean mesoscale eddy field and its air-sea feedbacks are better represented in high-resolution climate models (Bishop et al., 2017; McClean et al., 2011; Small et al., 2019). In this study, we use a high-resolution version of the Community Earth System Model (Hurrell et al., 2013), which will be referred to as Community Earth System Model-H (CESM-H). The ability to simulate regional EHFs in CESM-H has been tested in the studies of the Kuroshio Extension (Bishop et al., 2015), Southern Ocean (Bishop et al., 2016), and the Eastern Pacific Abernathey and Wortham (2015). The analysis in Abernathey and Wortham (2015) found good agreement between surface EHFs in CESM-H and observations in wavenumber-frequency space, but their study was isolated to a relatively quiescent region of the ocean away from strong western boundary currents. In this work, we adopt the same model simulation, but use a much longer 35-year span of time, which is described in Small et al. (2014), to analyze the surface divergent EHFs globally and compare it with observations.

The primary objective of this study is to reconstruct the global surface divergent EHFs using long-term satellite observations and compare against CESM-H. This paper is organized as follows. The methods are summarized in Section 2. The data used in this work, including satellite observations and model outputs, are described in Section 3. The results of global and regional EHFs are shown in Section 4. Discussions and conclusions on the results are given in Sections 5 and 6.

## 2. Methods

## 2.1. Surface Eddy Heat Flux

The surface EHF by the geostrophic flow is defined as the time-averaged product between SST anomaly and geostrophic velocity anomalies,  $\mathbf{v}'T'$ , where prime indicates a deviation from the monthly climatology and bar is the overall time average. Eddy-induced mixing is vital for closing the global ocean mixed layer heat budget

GUO AND BISHOP 2 of 19



(Greatbatch et al., 2007), which motivates us to estimate the mixed-layer EHF and transport in this study following Abernathey and Wortham (2015). By considering a climatological mixed layer depth, the mixed-layer transport of heat induced by eddies Q is written as follows:

$$Q = \rho_0 c_p \overline{\mathbf{v}'T'} H,\tag{1}$$

where  $\rho_0(\approx 1027 \text{ kg m}^{-3})$  and  $c_p(\approx 4000 \text{ J kg}^{-1}{}^{\circ}\text{C}^{-1})$  are two constants for ocean density and specific heat at constant pressure, respectively, and H is the mixed layer depth. The calculation in Equation 1 assumes uniform profiles of temperature and velocity within the mixed-layer. This assumption holds well in midlatitudes at the Kuroshio Extension Observatory for SST (M. F. Cronin et al., 2013). It is challenging to determine the vertical structure of the mixed layer temperature and geostrophic velocity field at the needed spatiotemporal resolutions from observations. At submesoscale fronts in the mixed layer the currents are likely in turbulent thermal wind balance (McWilliams et al., 2015; Wenegrat et al., 2018), also introducing additional processes that should be noted and are missing from our analysis. Our focus is on the mesoscale and in this study we are merely using Equation 1 to illustrate the typical magnitudes of the upper ocean eddy heat transport and to compare observational and model-based estimates.

#### 2.2. Helmholtz Decomposition

The EHF can be rewritten into two terms (rotational and divergent) using a Helmholtz decomposition,

$$\overline{\mathbf{v}'T'} = \mathbf{k} \times \nabla \psi + \nabla \phi, \tag{2}$$

where **k** is the vertical unit vector.  $\psi$  is like a velocity stream function, except for EHF, and  $\phi$  is a scalar potential. The curl of the gradient of  $\psi$  is regarded as the rotational component and the gradient of  $\phi$  indicates the divergent component. By taking the divergence of Equation 2, a two-dimensional Poisson equation is derived:

$$\nabla^2 \phi = \nabla \cdot \overline{\mathbf{v}'T'}.\tag{3}$$

We are able to estimate the divergent component of the EHF by solving the 2D Poisson equation Equation 3 and remove the nondynamic rotational flux from the total flux to clarify the actual meridional transport. Jayne and Marotzke (2002) solved the equation globally for scalar potential ( $\phi$ ) by inverting the divergence of EHF with a Laplacian inverter and applying Neumann boundary conditions, which indicates no flux on the boundary. Attempts have also been made by Aoki et al. (2013) to solve the Poisson equation with no normal flux on the boundaries to isolate the divergent eddy heat transport. However, their analysis was carried out over a relatively short time period (5 years) and in an uncoupled model simulation. We aim to extend our analysis to a much longer time period and in a coupled framework. It has been shown that the Helmholtz decomposition is not unique in a bounded domain with boundary conditions (Fox-Kemper et al., 2003). However, we find that our global decomposition is not sensitive to the choice of boundary conditions. Similarly, Lau and Wallace (1979) decomposed eddy fluxes in the global atmosphere and showed that their solutions were not sensitive to boundary conditions. The sensitivity of the solution to different boundary conditions in our analysis is examined and shown in Appendix A.

We aim to solve the Poisson equation on a fine grid with daily data for more than 25 years in this work, both accuracy and efficiency need to be considered to obtain valid and fast converging results. Several different mathematical algorithms have been compared. Traditional iterative methods for solving linear system equations were tested, such as Jacobi and Successive Over-Relaxation. In addition, an algebraic multigrid solver in Python was tested to solve Equation 3 with the scalar potential following Abernathey and Cessi (2014). All these methods have the same converged solutions with different computing speeds and memory requirements, but mainly these algorithms are too slow for large long-term data sets. The best method we found uses the function spsolve() in Python, which manipulates large sparse matrices to solve a linear system. This method increases computational efficiency.

GUO AND BISHOP 3 of 19



#### 2.3. Baroclinic Conversion Rate

Baroclinic Conversion (BC) rates are used to compare EHFs and their impacts on eddy-mean flow interactions in the mixed layer. The large-scale oceanic kinetic energy and available potential energy can be converted into smaller eddy scales through eddy-mean flow interactions. Baroclinic instability is a dominant mechanism for the formation of eddies near strong frontal jets and it indicates the energy transfer from Mean Potential Energy (MPE) to EPE. To quantify the potential energy conversion between the mean flow and eddies, the BC rate is calculated as follows:

$$BC = -\frac{\alpha g}{\theta_z} \overline{\mathbf{v}'T'} \cdot \nabla \overline{T} \tag{4}$$

where  $\alpha$  is the thermal expansion coefficient taken to be  $2 \times 10^{-4}$ °C<sup>-1</sup>, g is the gravitational acceleration.  $\overline{\theta_z}$  is the averaged vertical gradient of potential temperature at the base of mixed layer (which is defined as the level at which the surface temperature drops by 0.2°C based on Monthly Isopycnal & Mixed-layer Ocean Climatology (MIMOC) potential temperature. MIMOC data set is described in the next section). The overbar on EHFs and temperature gradient denotes the time mean over the data set record. Positive BC indicates a conversion from MPE to EPE and a negative BC vice versa. We additionally adopt the units of BC as cm<sup>2</sup> s<sup>-3</sup> in this work following M. Cronin and Watts (1996); Bishop et al. (2013).

#### 3. Data

In this section, we document the observational data sets used to quantify Equations 1 and 4 and describe the high-resolution climate model data to compare against.

#### 3.1. Sea Surface Height and Geostrophic Velocity

The merged absolute dynamic topography (ADT) product derived from satellite altimetry is used in our analysis. The gridded ADT data set is distributed by Copernicus Marine and Environment Monitoring Services and is available daily from January 1993 to the present at a spatial resolution of  $0.25^{\circ} \times 0.25^{\circ}$ . In order to compute EHF, we use precomputed geostrophic velocity derived from the daily SSH product. This product is based on the geostrophic balance and has sophisticated treatment in the low-latitude regions where geostrophy fails (Lagerloef et al., 1999). In this work, we ignore the submonthly variability by using the monthly mean SSH and geostrophic velocity.

#### 3.2. Sea Surface Temperature

SST data from the NOAA  $1/4^{\circ}$  Optimum Interpolation Sea Surface Temperature version 2 are used to estimate surface EHFs. This product is an analysis constructed by combining observations from satellites, ships, buoys, and Argo floats (Reynolds et al., 2007). It shares the same geographic grid and spatial resolution of quarter degree with the geostrophic current mentioned above, and is daily sampled beginning from 1981 to the present. We use the monthly SST for the same time frame 1993–2017 as the altimeter data.

## 3.3. Mixed Layer Depth

In order to estimate EHFs in the mixed layer, the MIMOC data is used to provide climatological mixed layer information including the monthly mean mixed layer depth and a background vertical thermal gradient. This product is mainly based on Argo Conductivity, Temperature and Depth profile (CTD) data, supplemented by shipboard and Ice-Tethered Profiler CTD data with 1° resolution (Schmidtko et al., 2013). A linear interpolation is applied to remap onto the same spatial grids to match the data set of SST and SSH.

## 3.4. Observation-Based ARMOR3D Product

ARMOR3D is a global 3D weekly temperature, salinity, and geostrophic velocities fields at a spatial 0.25° resolution by combining satellite observed sea level anomaly, SST, and salinity data sets with in situ temperature and

GUO AND BISHOP 4 of 19

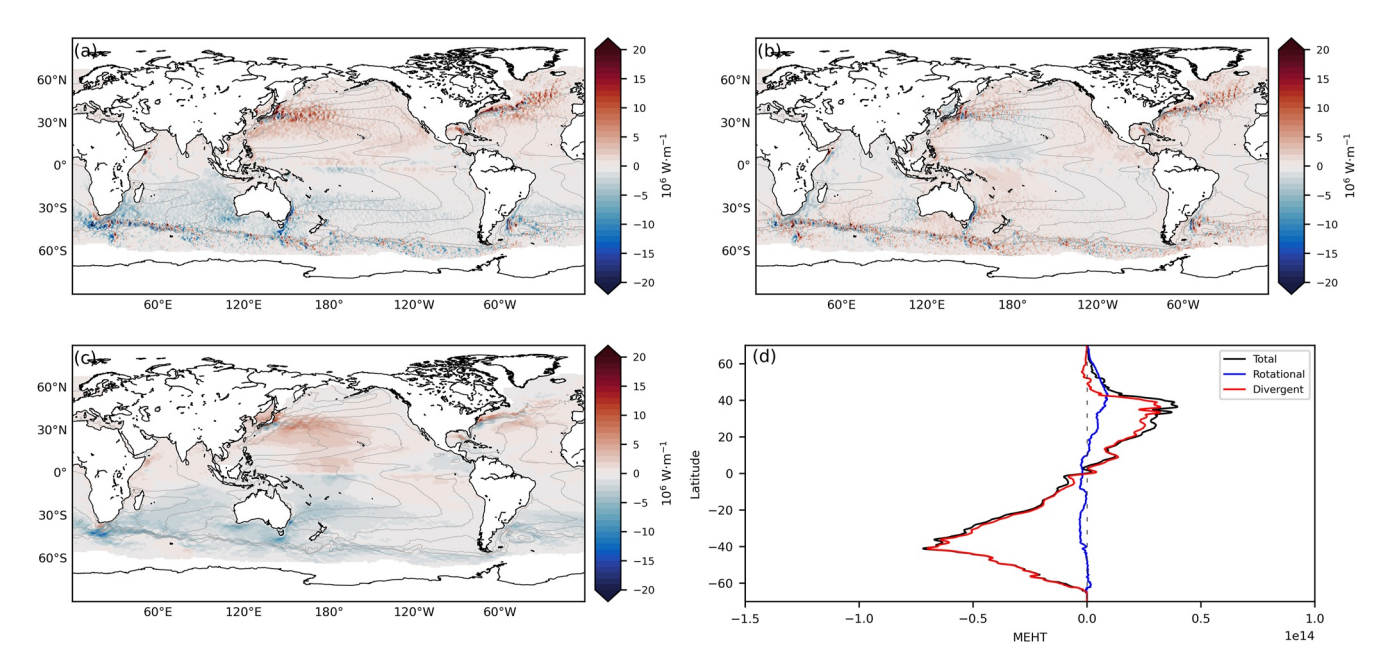


**Figure 1.** Global mixed layer vertically integrated meridional eddy heat flux from satellite observations from 1993 to 2017. Top left: full flux; Top right: rotational component; Bottom left: divergent component; Gray contours are the mean sea surface height contours (CI = 0.2 m). Bottom right: Zonal integration of  $Q^y$ ,  $Q^y_{rot}$  and  $Q^y_{div}$  in unit of Watt.

salinity vertical profiles (Guinehut et al., 2012; Mulet et al., 2012; Verbrugge et al., 2017). This product has been successfully applied to studies in the Gulf Stream and the reliability was evaluated in Chi et al. (2018). In this work, ARMOR3D is only used to support the discussion section on interpreting the divergent EHF field in the Kuroshio Extension and Gulf Stream to produce Figure 14 in Section 5.

## 3.5. High-Resolution Climate Model (CESM-H)

The climate model analyzed here is a new state-of-the-art high-resolution version of the Community Earth System Model, which was performed for 100 years with 14 years of spinup (Small et al., 2014). The model is composed of the Community Atmosphere Model version 5 (CAM5) (Park et al., 2014), Parallel Ocean Program version 2 (POP2) (Smith et al., 2010), Community Ice Code version 4 (Hunke et al., 2010), and Community Land Model version 4 (Lawrence et al., 2011). The ocean component POP2 has a nominal grid spacing of  $0.1^{\circ}$  with 62 vertical levels. The atmospheric model CAM5 has horizontal resolution of  $1/4^{\circ}$  with 30 levels in the vertical. In this study, we use the monthly model output of 35 years from year 45 to year 80. In order to make it consistent with the resolution of observational data set, spatial subgriding was performed and new fields were remapped to horizontal resolution of  $0.25^{\circ}$ . Note that we only isolate the geostrophic components of the motion in the CESM-H to make a more direct comparison with the observational-based results in this work. The geostrophic velocity anomaly is calculated from the SSH anomaly  $\eta'$ ,  $\mathbf{v}' = g/f \, \mathbf{k} \times \nabla \eta'$ , where f is the Coriolis parameter. For all model analyses in this study, equatorial band  $(5^{\circ}\text{S}-5^{\circ}\text{N})$  has been masked out where geostrophic balance does not hold well.

#### 4. Results

## 4.1. Global Mixed-Layer Divergent Meridional Eddy Heat Transport

The global distribution of surface EHFs is shown in Figure 1. Figure 1a shows the 25-year (1993–2017) averaged mixed-layer meridional EHF  $(Q^y)$ , computed using Equation 1. A large contribution of poleward eddy transport of heat comes from the western boundary currents and Antarctic Circumpolar Current.  $Q^y$  displays a wave-like pattern with positive and negative values alternating in the downstream direction, especially in regions with strong zonal mean flow, such as in the Gulf Stream, Kuroshio Extension, and Antarctic Circumpolar Current. After applying the Helmholtz decomposition to the global Q, the rotational  $(Q^y_{rot})$  and divergent  $(Q^y_{div})$  components are distinguished and shown in Figures 1b and 1c, respectively. By removing the rotational component from

GUO AND BISHOP 5 of 19

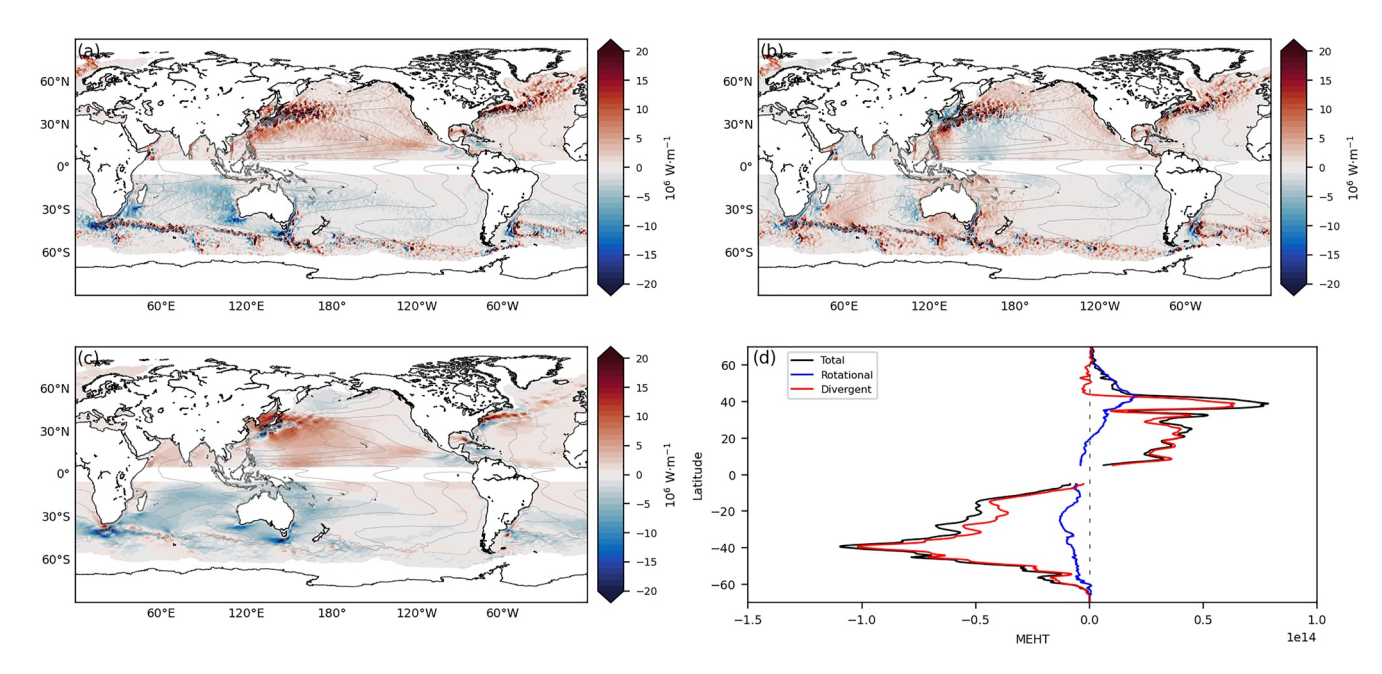


Figure 2. Same as Figure 1 but for model data.

the full fluxes, a spatially coherent map appears for  $Q_{div}^y$ , which eliminates the meandering structure along the zonal jets. Similar to  $Q^y$ ,  $Q_{div}^y$  is largest in the western boundaries, Antarctic Circumpolar Current as was found in Jayne and Marotzke (2002) and Aoki et al. (2013).

In general, the time-averaged ocean surface heat transport by eddies is poleward except for a few regions where strong divergence pattern occurs. In these divergence regions there is equatorward surface EHFs that occur along the southern flanks of both the Kuroshio Extension and Gulf Stream. Equatorward surface EHFs are only observed in the northern hemisphere western boundary current. This too was also obtained for depth-integrated eddy heat transport estimates from an eddy-resolving ocean general circulation model (Aoki et al., 2013). The proposed mechanism described in Aoki et al. (2013) is due to the interaction between propagating meanders and cyclonic eddies that detach from the Kuroshio and Gulf Stream, and the southward velocity anomaly induced by these mesoscale features advects warm anomalous water to the south, resulting in an equatorward EHF. This will be further explored in Section 5 with an observational-based data set. The zonally integrated mixed-layer meridional eddy heat transport is shown in Figure 1d, where the divergent component appears to be similar to that of the full transport and suggests that the rotational component does not contribute to the integrated poleward transport of heat. Although the integrated rotational fluxes are still shown to be nonzero in Figure 1d, which may originate from the numerical error of solving the Poisson equation, the divergent component extracted here captures the overall distribution of the globally integrated meridional EHFs. The error map of the decomposition and its sensitivity to two different boundary conditions are provided in Appendix A.

Similarly, the ocean mixed-layer meridional EHF and its decomposition were calculated with the high-resolution CESM output as shown in Figure 2. The  $Q^y$  displays good consistency with that derived from observations in terms of their geographic distributions. The largest poleward divergent fluxes are concentrated near the western boundary currents and Antarctic Circumpolar Current, and the zonally integrated divergent EHF is comparable to the total transport. Based on the zonal integrals of EHF, mixed-layer mesoscale processes contribute up to 0.07 PW (1PW =  $10^{15}$ W) and 0.1 PW in the midlatitudes in the observations and CESM-H, respectively. The relatively higher magnitude in the CESM-H is also coincident with larger SST and SSH variance in the climate models (Small et al., 2014). A detailed regional comparison regarding EHFs in the CESM-H and observations is discussed in Section 4.2.

The BC rates (Equation 4) are used to estimate the energy transfer in the mixed layer between the MPE and EPE. The global distribution of long-term BC rate derived from observations is shown in Figure 3a. BC is overwhelmingly positive and downgradient in accordance with baroclinic instability (Equation 4), however, there

GUO AND BISHOP 6 of 19

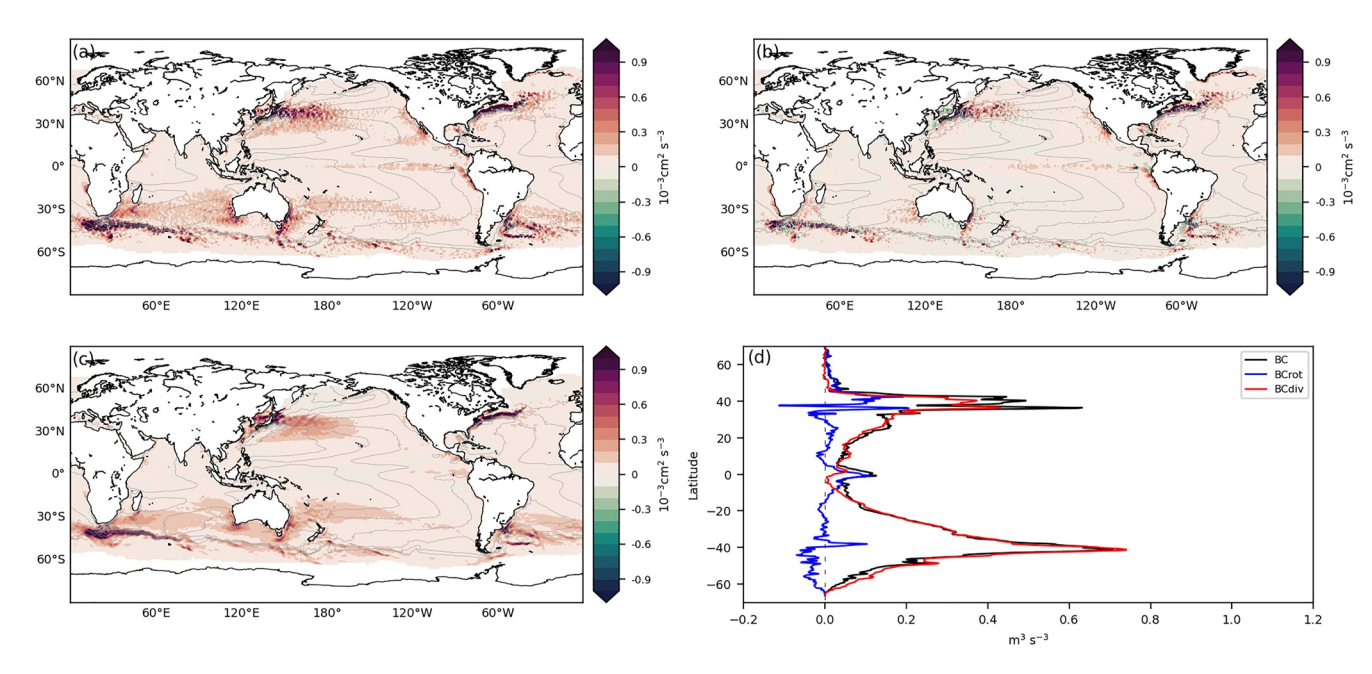


Figure 3. Global mean baroclinic conversion rates at the surface with units of cm $^2$  s $^{-3}$  from observation from 1993 to 2017. Top left: BC; Top right: BC<sub>rot</sub> associated with rotational flux; Bottom left: BC<sub>div</sub> associated with divergent flux; Bottom right: zonal integrals of BC, BC<sub>rot</sub>, BC<sub>div</sub>. Gray contours indicate sea surface height (CI = 0.2 m).

are notable along-stream wave-like alternating positive and negative values within the major western boundary currents and Southern Ocean. These alternating features are due to the meandering of the currents and result in upgradient fluxes that are nondynamical in a sense that they do not result in any net energy conversion (Jayne & Marotzke, 2002). These unrealistic upgradient fluxes in the rotational component of EHFs (associated with negative conversion rates) should be largely balanced by the advection of EPE (Marshall & Shutts, 1981). We can remove the upgradient fluxes by utilizing the Helmholtz decomposition demonstrated in Figure 1. The BC rates associated with rotational and divergent fluxes are shown in Figures 3b and 3c, respectively. A smoothed spatial distribution of BC resulting from the divergent EHF field is largely confined to the midlatitudes western boundary currents and Antarctic Circumpolar Current, where strong eddy-mean flow interaction occurs. Globally, the BC<sub>div</sub> is mostly positive as in Figure 3d. The latitude-dependent distribution of the BC<sub>div</sub> closely follows the total BC, suggesting that the rotational flux does not contribute significantly to the global energy budget.

We further examined the global BC rate in the CESM-H (Figure 4). In general, BC distribution in the model shows strong consistency with the estimate in observations. For example, the strongest positive conversions appear along the northern hemisphere western boundary currents and Southern Ocean Antarctic Circumpolar Current. The zonally integrated BC<sub>div</sub> corresponds closely to the total indicating the model BC<sub>rot</sub> also has no large contribution to the global energy budget as in the observations (Figure 3d). The stronger mixed-layer EHFs in the model (Figure 2) contribute to higher BC rates, especially in the Kuroshio Extension and Gulf Stream (see Section 4.2.1). To compare with the global full-depth-integrated Lorenz energy cycle in Von Storch et al. (2012), we adjust the unit of BC<sub>div</sub> into TW (1 TW =  $10^{12}$ W) by multiplying the climatological mixed layer depth H, a reference density  $\rho_o$  and integrating across the globe. The generation of EPE through BC reaches 0.11 TW in the observations and 0.16 TW in the model. These mixed layer values are approximately 20% of the global full-depth estimates (0.83 TW) in Von Storch et al. (2012), showing the importance of the near surface ocean circulation in global energetics. Regional comparisons of the local BC<sub>div</sub> in the model and observations are discussed in the following section.

In addition to long-term mean distribution of surface EHFs-related energy conversion, we further investigated its spatiotemporal dependence by adopting a similar method, which was used in Bishop et al. (2020) for investigating scales of diabatic EPE generations through air-sea interface. For space-scale dependence, a two-dimensional boxcar filter was used to smooth the anomaly surface velocity and temperature fields with box length increasing incrementally by  $0.5^{\circ}$  from  $0.5^{\circ}$  to  $10^{\circ}$ . To examine the time scale dependence, we low-pass filter the data sets

GUO AND BISHOP 7 of 19

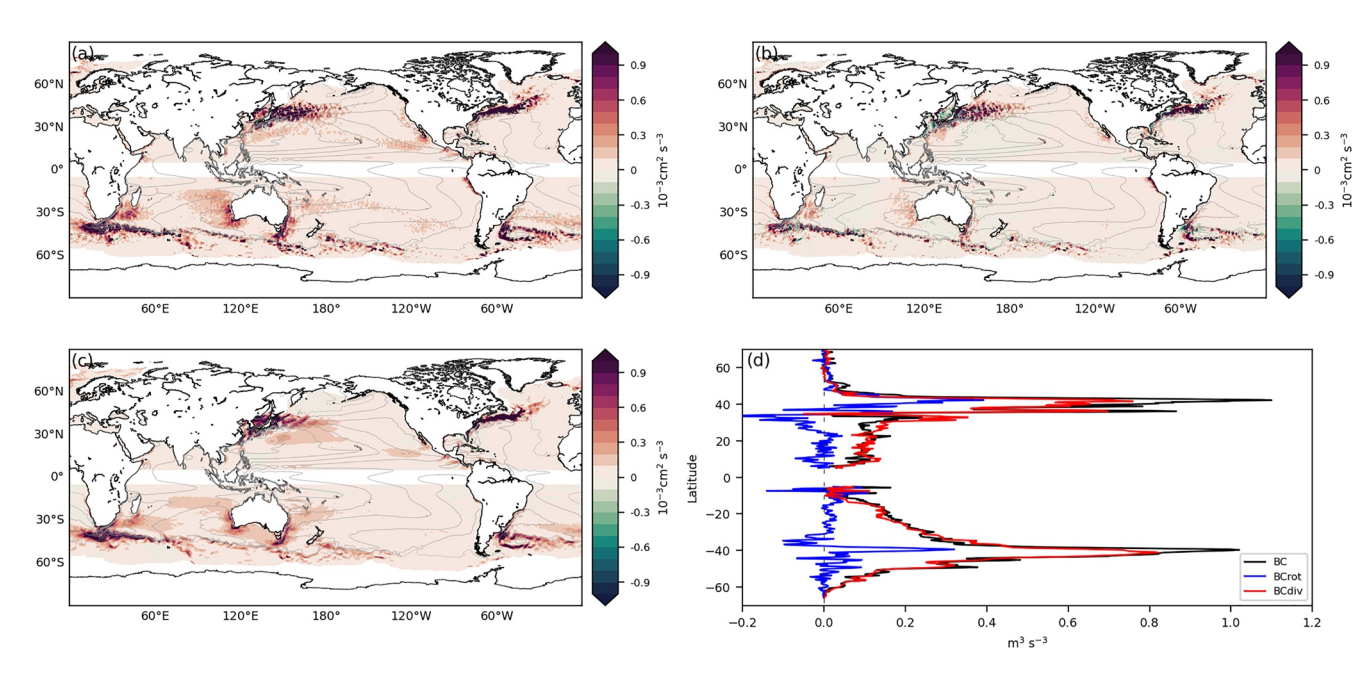


Figure 4. Baroclinic conversion rates in Community Earth System Model-H. Panels (a-d) are the same as Figure 3 but for model data except ±5° of the equator is left blank

using a fourth-order Butterworth filter with cutoff frequencies increasing from 1/3 month<sup>-1</sup> to 1/60 month<sup>-1</sup> with an increment of 1/3 month<sup>-1</sup>. The ratio of global surface integrated BC rate based on filtered data to that based on unfiltered data is shown for both observations and CESM-H in Figure 5 after teasing out a tropical band (5°S–5°N). The observations and model have an identical distribution in terms of the scale dependence of global BC rate. For a time period longer than 2 years, only less than 20% of the BC remains at all space scales. The BC filtered to unfiltered ratio is reduced to 10% at timescales longer than 4 years in the observations and 5 years in the CESM-H, which implies a stronger variability at long timescales in the model. As spatial scales are successively smoothed, both observations and CESM-H show 90% of the MPE-EPE conversion are maintained by length scales shorter than ~4.5° and half of the BC is constrained within ~1.5°. Overall, it is found in Figure 5 that 80% of the MPE-EPE conversion is confined to timescales less than 2 years and length scales less than 4°, where the mesoscale band locates.

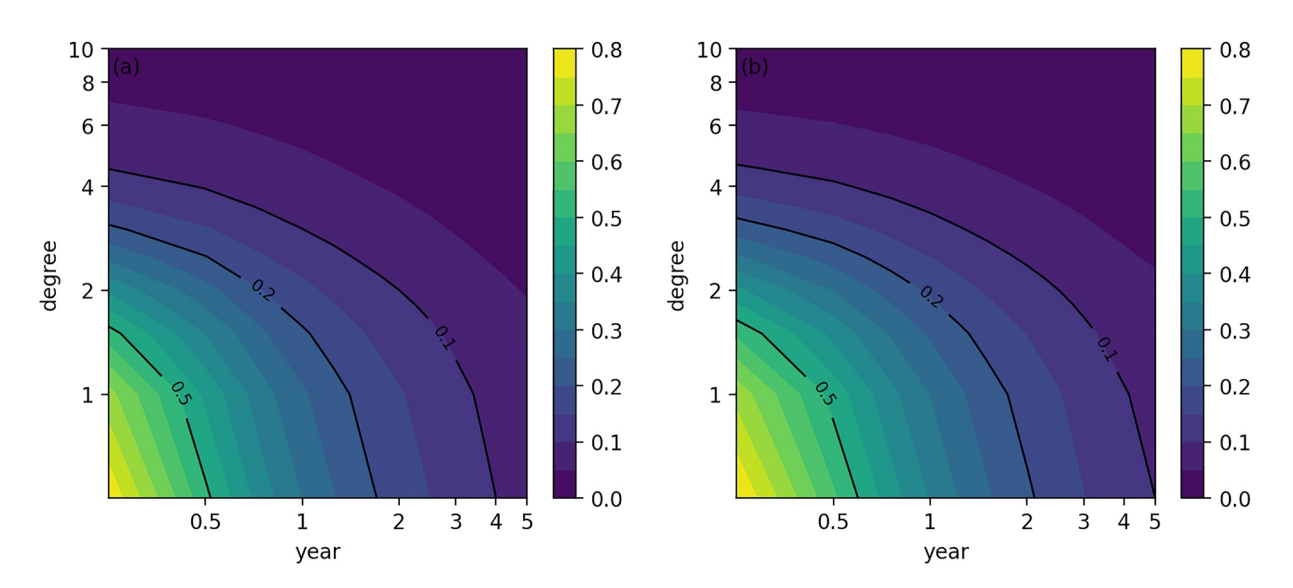


Figure 5. Spatiotemporal scale dependence of the global surface integrated Baroclinic Conversion (BC) rate represented as a ratio of BC between using filtered data and using unfiltered data on a log-log scale. (a) Observations and (b) Community Earth System Model-H.

GUO AND BISHOP 8 of 19



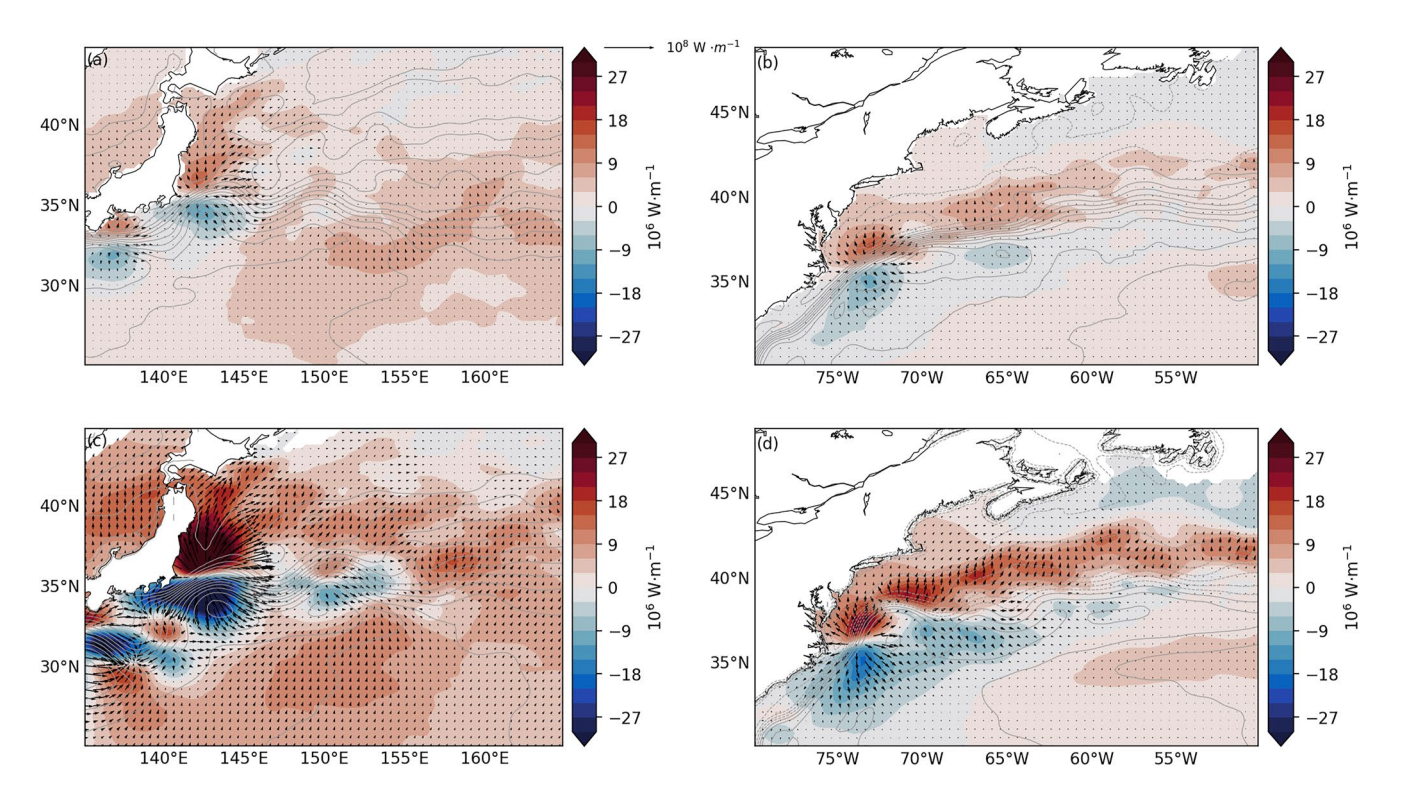


Figure 6. Mean divergent meridional eddy heat transport in the mixed layer for Kuroshio Extension (panels a and c) and Gulf Stream (panels b and d) from observations (upper panel) and CESM-H (lower panel). Q<sub>div</sub> vectors superimposed on its meridional component. Gray contours indicate sea surface height (CI = 0.1 m).

## 4.2. Regional Hotspots

## 4.2.1. Northern Hemisphere Western Boundary Currents

Figure 6 illustrates the long-term mean  $Q_{div}^y$  in the Kuroshio Extension and Gulf Stream from the observations and CESM-H. Although similar spatial patterns are seen between the model and observations, the mixed-layer EHF has a larger magnitude in the model. As a comparison, the poleward divergent EHF  $Q_{div}^y$  in the Kuroshio Extension (25°N–45°N, 135°E–165°E) averages 3.2 MW m<sup>-1</sup>(1 MW = 10<sup>6</sup>W) and peaks at 13.3 MW m<sup>-1</sup> adjacent to the coast, while the corresponding values shown in the model are 7.6 MW m<sup>-1</sup> and 47.7 MW m<sup>-1</sup>. In the Gulf Stream (30°N–50°N, 80°W–50°W), the mean  $Q_{div}^y$  is approximately 2.4 MW m<sup>-1</sup> in the observations and 4.5 MW m<sup>-1</sup> in CESM-H. The strongest northward transport in the Gulf Stream is found near the separation area with values of 15.6 MW m<sup>-1</sup> and 25.6 MW m<sup>-1</sup> for the observations and CESM-H, respectively.

The spatial structure of the divergent BC rates in the two current systems is shown in Figure 7 for both the observations and CESM-H. The long-term BC<sub>div</sub> shows positive conversions from mean to EPE in these regions. The maximum BC<sub>div</sub> reaches  $3.6 \times 10^{-3} \text{cm}^2 \text{ s}^{-3}$  along the first crest of the Kuroshio Extension on the northern side of the current where SST gradients are prominent. The average value for the region  $(25^{\circ}\text{N}-45^{\circ}\text{N}, 135^{\circ}\text{E}-165^{\circ}\text{E})$  is approximately  $3 \times 10^{-4} \text{cm}^2 \text{ s}^{-3}$ . The Gulf Stream has similar values and also has a maximum on the northern side of the current. However, the BC rates extend further downstream than in the Kuroshio Extension and may be related to stronger SST gradients in the Gulf Stream. Both the Kuroshio Extension and Gulf Stream have surface values that are two times smaller than what has been reported for the thermocline depth (Bishop et al., 2013; M. Cronin & Watts, 1996).

Although the surface EHFs in the CESM-H share good agreement in terms of spatial distributions with those in the observations, the magnitude in the coupled model is larger than that in the observations, especially in the Northern Hemisphere western boundary currents. The relative difference in the covariance  $\overline{\mathbf{v}'T'}$  spanning different timescales between the model and observations was explored from a cross-spectrum analysis. We selected a few points near the flux hotspots in the Kuroshio Extension (Figure 8) and Gulf Stream (Figure 9) and applied the cross-spectrum method with a Hanning window. The overall spectral density in the Kuroshio Extension and

GUO AND BISHOP 9 of 19



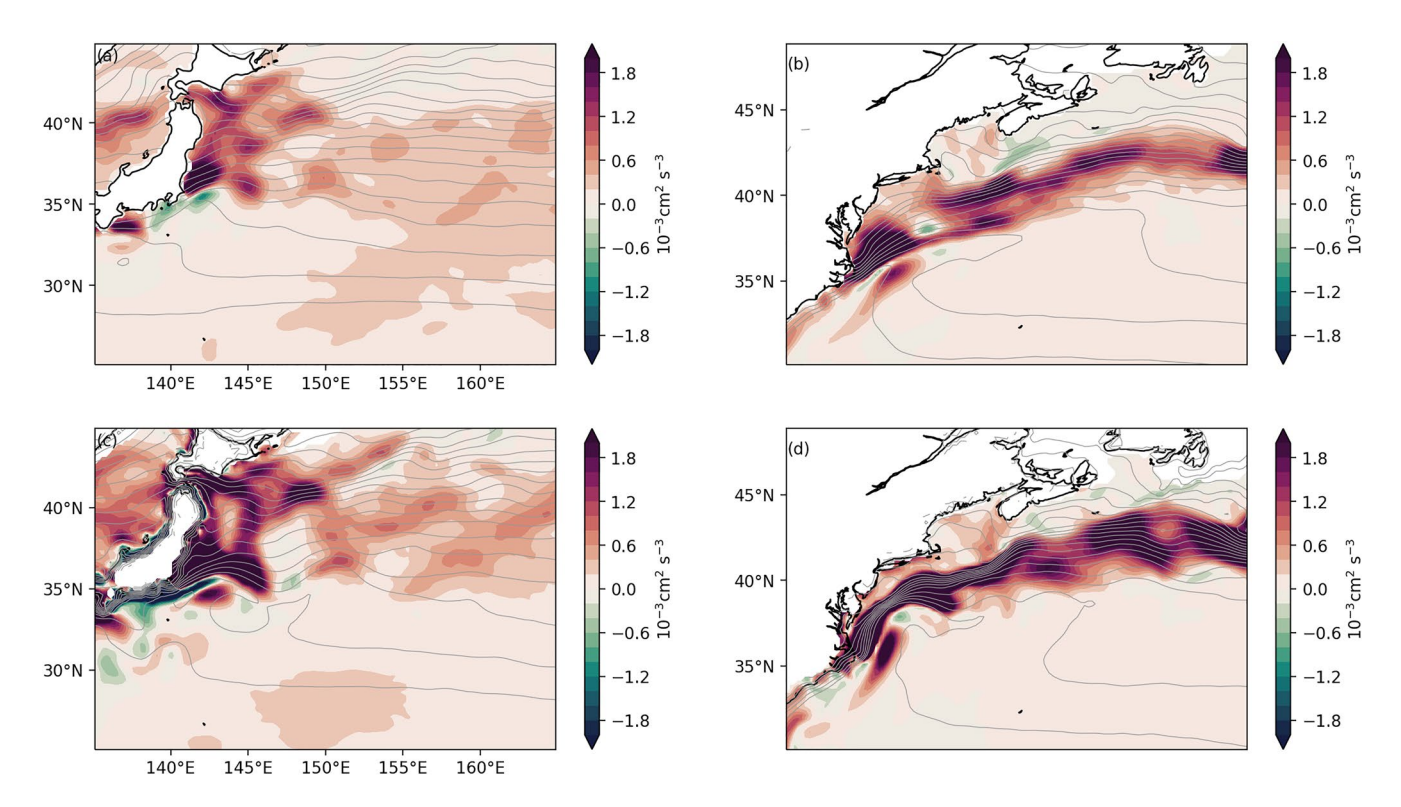
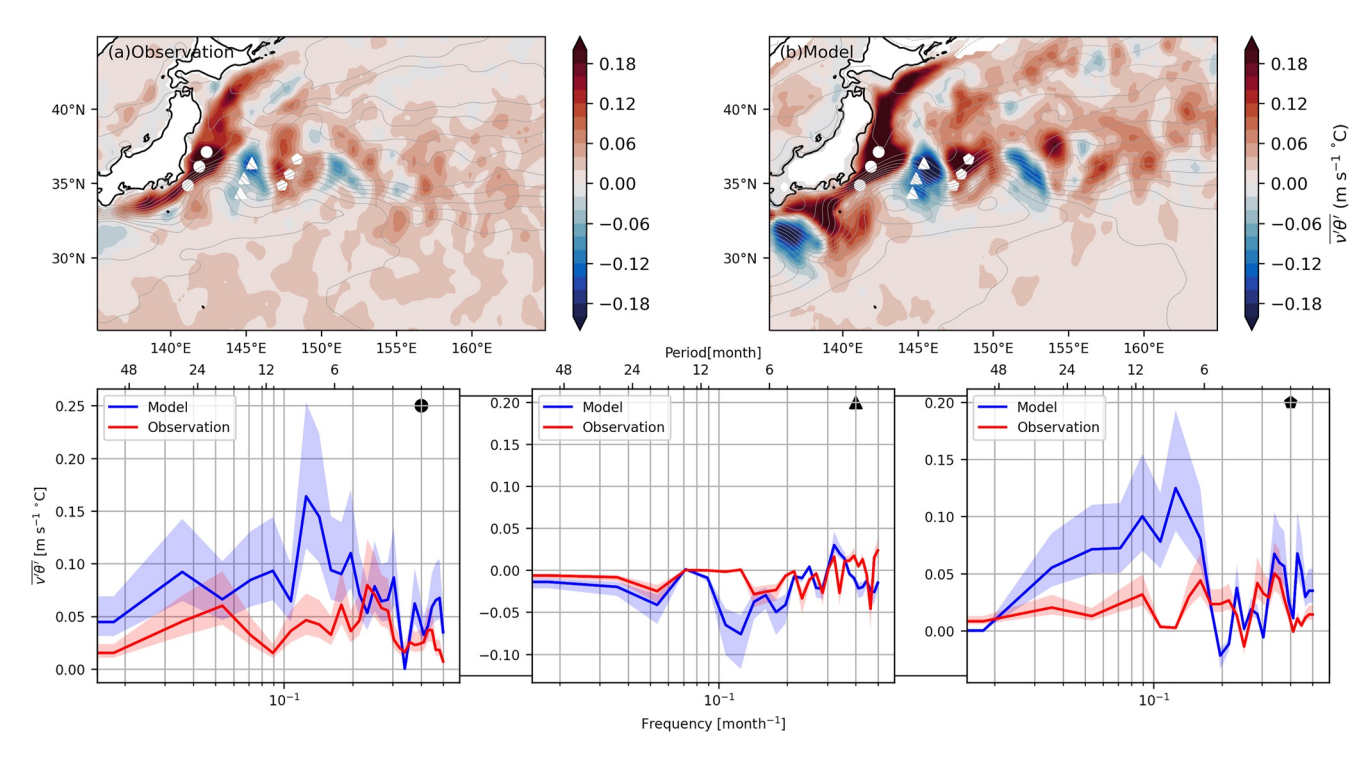


Figure 7. Mean surface divergent component of baroclinic conversion rates for the Kuroshio Extension (panels a and c) and Gulf Stream (panels b and d) from observations (upper panel) and Community Earth System Model-H (lower panel). Sea surface temperature contours are overlaid as a reference with  $CI = 1^{\circ}C$ .



**Figure 8.** Top panel: averaged surface eddy heat flux ( $\mathbf{v}'T'$ ) in the Kuroshio Extension based on (a) observation and (b) model. Bottom panel: cross-spectrum of  $\mathbf{v}'T'$  averaged for the points with same marker. Gray contours indicate sea surface height (CI = 0.1 m). Cross-spectrum is performed for segment length of 56 months and 50% overlap. The shaded region denotes the 95% significance interval at each frequency.

GUO AND BISHOP 10 of 19

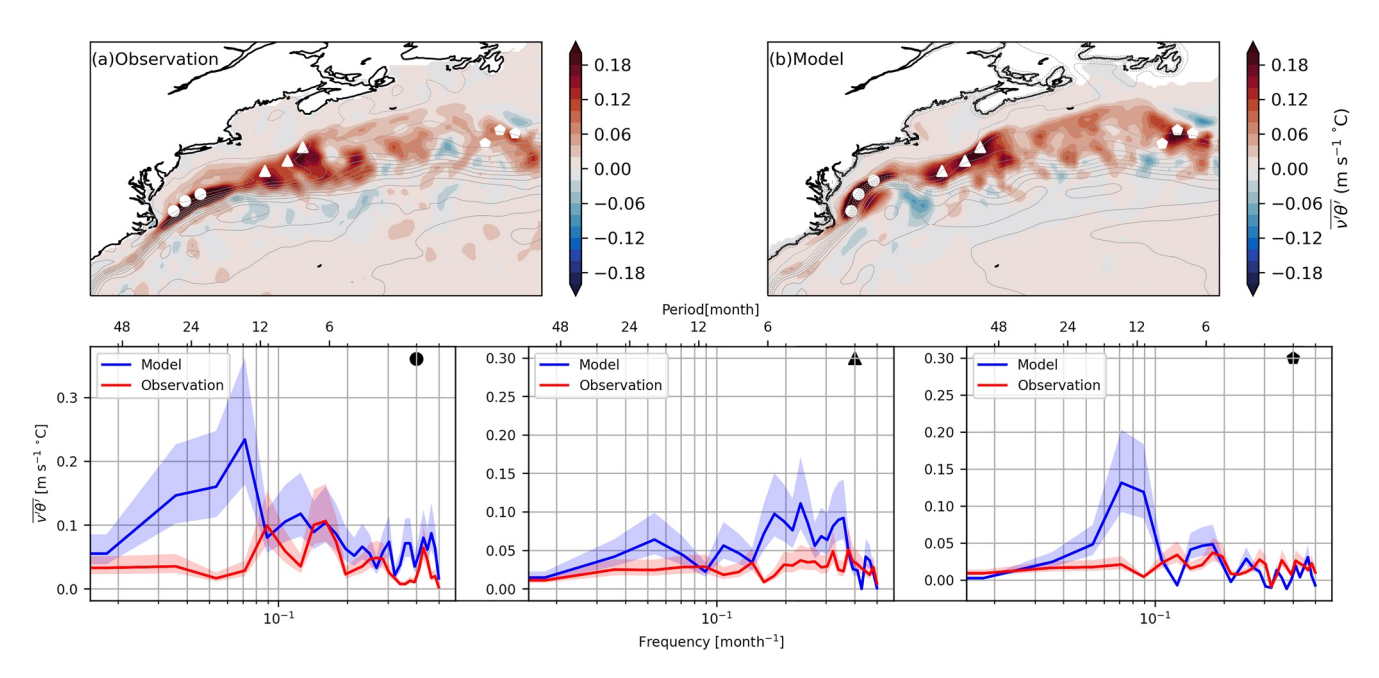


Figure 9. Same as Figure 8 but for the Gulf Stream.

Gulf Stream from CESM-H is higher than that in the observations. In the Kuroshio Extension, we chose three subregions that have strong fluxes along the mean zonal path; the first meander crest, the first meander trough, and the second meander crest. For the spectrum near the first crest (marked by circles in Figure 8), the model has the largest energy over a period of 8 months, where the observations also capture one small peak on this band. The observations overall have comparable magnitude of covariability between eddy velocity and temperature within the frequency band higher than 1/6 month<sup>-1</sup> near the meander crest along the Japan coast. The CESM-H has a larger variance within the low-frequency band than the observations. At the meander trough (marked by triangles in Figure 8), the cross-spectrum in the model also shows stronger flux variability than the observations at the period longer than 6 months. Similarly, near the second meander crest (marked by pentagons in Figure 8), the EHF is much stronger in long timescales in the CESM-H by comparing the cross-spectrum between the model and observations. For the two subregions with hot spots of positive EHFs appearing close to the meander crests, the CESM-H has almost two times higher energy in the low-frequency band than the observation, while the model agrees well with the observations for the frequency band higher than 1/6 month<sup>-1</sup>. For the flux hot spots close to the meander trough, the model matches better with the observations from the cross-spectrum results. Same conclusion can be drawn in the Gulf Stream, where a higher spectral density is captured in the CESM-H (Figure 9) especially for frequencies lower than 1/10 month<sup>-1</sup>. In summary, the dominant timescales of EHFs revealed by the observations and CESM-H in these regions are quite similar, although the model has a relatively larger magnitude for the low-frequency bands.

## 4.2.2. Southern Ocean

In the southern hemisphere  $Q^y_{div}$  is primarily poleward with the western boundary current systems making up the largest contribution to meridional eddy heat transport and BC rates with the exception of south western Australia and portions of the Antarctic Circumpolar Current. The geographic distribution of  $Q^y_{div}$  in the Southern Ocean is shown in Figures 10a and 10b for the observations and CESM-H. In the Agulhas Return Current, the observations and CESM-H share the same geographic distributions, but with increased heat transport in the model with mean poleward transport of 2.2 MW m<sup>-1</sup> and 3.8 MW m<sup>-1</sup>, respectively, in the region of 50°S–30°S, 10°E–70°E. In the East Australian current (50°S–30°S, 145°E–170°E), the mean poleward transport of  $Q^y_{div}$  is approximately 2.8 ~ 3.1 MW m<sup>-1</sup> in the observations and model with a stronger flux in southern Tasmania in CESM-H. In the Brazil-Malvinas confluence zone (50°S–30°S, 60°W–25°W), the CESM-H has a relatively higher mean poleward flux of 2 MW m<sup>-1</sup> than 1.5 MW m<sup>-1</sup> in the observations. BC rates (BC<sub>div</sub>) are positive and shown in Figures 10c and 10d, which share a similar spatial distribution to  $Q^y_{div}$  (Figures 10a and 10b). The regional mean BC<sub>div</sub> for the Agulhas Return Current, East Australian Current, and Brazil-Malvinas Confluence from observations are 0.15,

GUO AND BISHOP 11 of 19



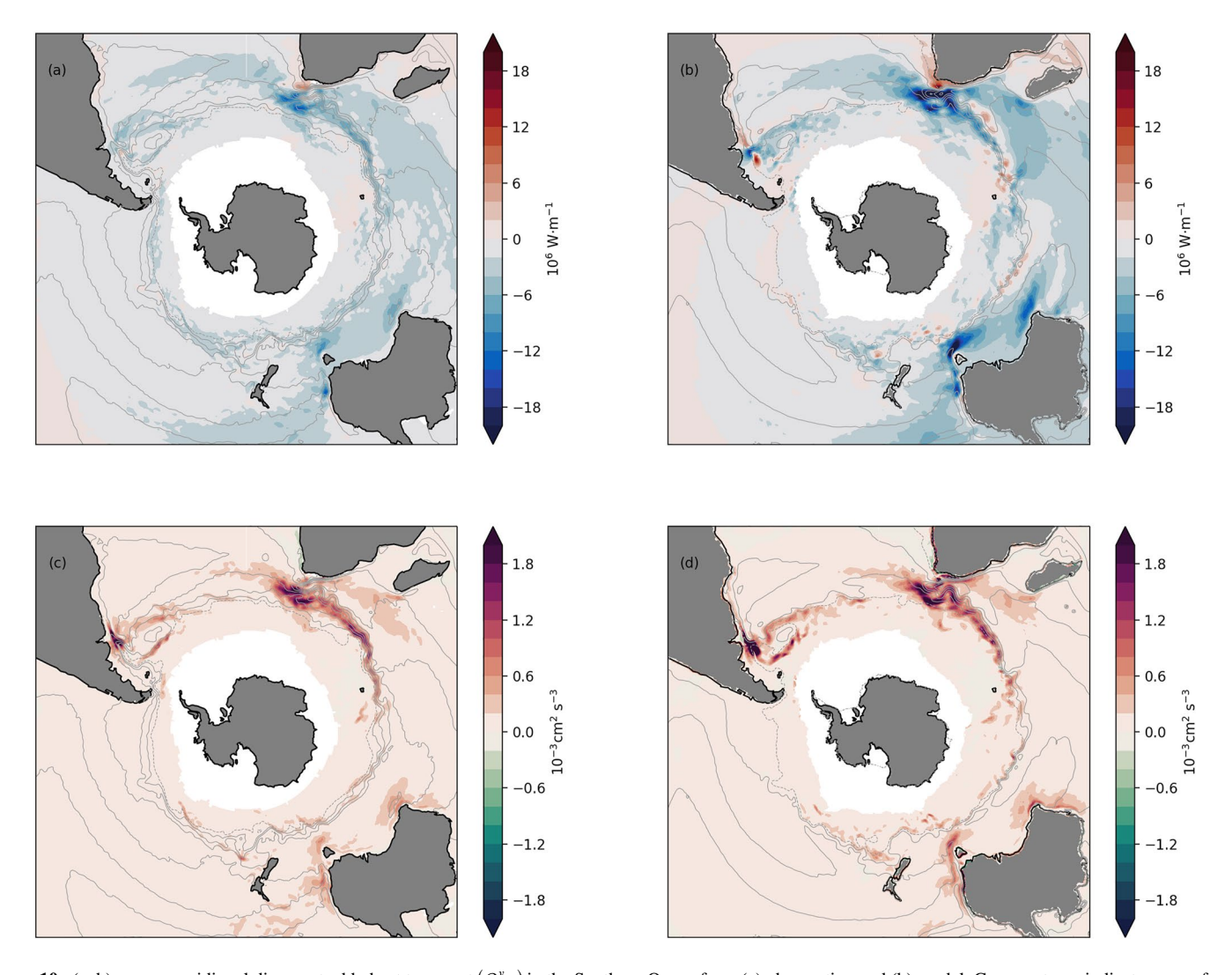


Figure 10. (a–b): mean meridional divergent eddy heat transport  $(Q_{div}^{J})$  in the Southern Ocean from (a) observation and (b) model. Gray contours indicate sea surface height (CI = 0.2 m). (c–d): mean surface divergent component of baroclinic conversion rates for the Southern Ocean from (c) observations and (d) Community Earth System Model-H. Gray contours indicate sea surface height (CI = 0.2 m).

0.17, and  $0.14 \times 10^{-3}$  cm<sup>2</sup> s<sup>-3</sup>, respectively; and the corresponding mean values in the CESM-H are 0.17, 0.17, and  $0.21 \times 10^{-3}$  cm<sup>2</sup> s<sup>-3</sup>, respectively, which show good agreement between the coupled model and observations.

For comparison with previous in situ EHFs measurements (Bryden & Heath, 1985; Ferrari et al., 2014; Phillips & Rintoul, 2000; Watts et al., 2016), we multiply the covariance  $\mathbf{v}'T'^{\text{div}}$  by  $\rho_0 C_p$  to adopt the unit of kW m<sup>-2</sup>. We find that our surface values are consistently smaller than subsurface thermocline estimates. The depth-averaged eddy heat transport measured by moorings deployed along the Drake Passage from 2006 to 2009 ranges from +21.2 KW m<sup>-2</sup> to -92.1 KW m<sup>-2</sup>, with several statistically nonsignificant equatorward fluxes (Ferrari et al., 2014). From Current and Pressure-equipped Inverted Echo Sounders deployed during Drake (2007–2011), Watts et al. (2016) found that at different depth levels, the EHFs were approximately -80 ~ -10 KW m<sup>-2</sup> across the Drake Passage. Our surface estimates in the Drake Passage region (66°W–60°W, 62°S–54°S) are close to -18.5 KW m<sup>-2</sup> on average, which is within the ranges evaluated in both Ferrari et al. (2014) and Watts et al. (2016). Within the Sub-Antarctic front south of Australia Phillips and Rintoul (2000) estimated EHFs and BC rates using a current meter array, and they showed that the heat flux has a magnitude of -91.9 KW m<sup>-2</sup> at 420 dbar for 4 moorings. At the same location (143°E, 50.5°S), the surface divergent EHFs are -45.7 KW m<sup>-2</sup>, with a corresponding BC rate of  $2.2 \times 10^{-4}$ cm<sup>2</sup> s<sup>-3</sup>.

GUO AND BISHOP 12 of 19



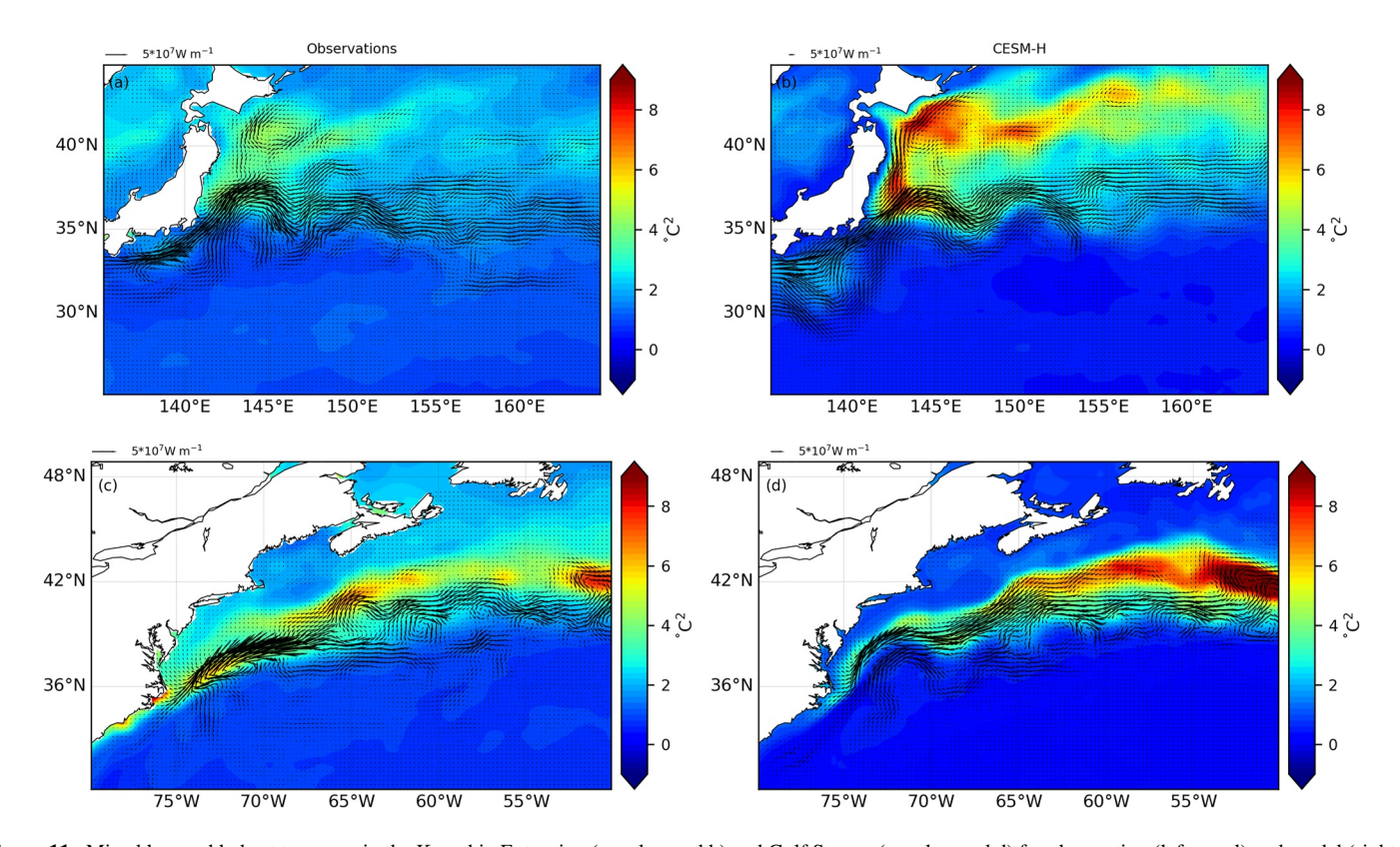


Figure 11. Mixed layer eddy heat transport in the Kuroshio Extension (panels a and b) and Gulf Stream (panels c and d) for observation (left panel) and model (right panel). Color denotes surface temperature variance and arrows indicate eddy heat transport vector.

## 5. Discussion

In baroclinically unstable regions the conversion of EPE mainly originates from the vertical eddy buoyancy fluxes, which converts EPE to EKE, the mean advection of EPE (Marshall & Shutts, 1981) and mesoscale air-sea interaction (Bishop et al., 2020; Ma et al., 2016). Following Marshall and Shutts (1981), BC<sub>res</sub> balances the mean advection of EPE if the geostrophic velocity field is equivalent barotropic, meaning the velocity is vertically aligned with the buoyancy field, which shows that there is a linear relationship between the geostrophic stream function and buoyancy field (Bishop et al., 2013; Killworth, 1992). And BC<sub>div</sub> can balance the conversion of EPE to EKE in an adiabatic framework. That infers that the rotational flux may circulate around the temperature variance contours (Bishop et al., 2013; M. Cronin & Watts, 1996; Watts et al., 2016). To test the role of local rotational EHFs, a comparison of regional mixed-layer  $Q_{rot}$ ,  $Q_{div}$  between the observations and model is shown in Figure 11. The background temperature variance is underlain with transport vectors. It is shown that the wavelike structure displayed in the rotational flux generally circulates around the temperature variance. One prominent example is the anticyclonic circulation at approximately 146°E, 41°N in the Kuroshio Extension (Figure 11a). The spatial coherence between rotational fluxes and temperature variance infers that the rotational flux is associated with the mean flow advection of EPE to some extent and has no significant impact on eddy-mean flow interactions. The observational-based surface BC rates associated with the rotational flux in the Kuroshio Extension and Gulf Stream are shown as examples in Figure 12. The wave-like pattern dominates the distribution of  $BC_{rot}$  with unrealistic upgradient fluxes (negative values) along the jet paths.  $BC_{div}$  associated with divergent heat flux is quite different from BC<sub>rot</sub> and has smoothed spatial structures, where dominant positive values indicate the depletion of MPE by eddies (Figure 7). Therefore, the divergent component of the eddy buoyancy flux is the relevant flux for estimating local BC, and it is quite necessary for local energetics analysis to partition the EHF and remove the rotational conversions.

It is noticed that the observed SST variance has a similar geographical distribution with the model outputs in the Kuroshio Extension and Gulf Stream (Figure 11), while the model has a larger variance compared with the observations, especially for the region off of Japan and north of the jet path in the Kuroshio Extension. This

GUO AND BISHOP 13 of 19

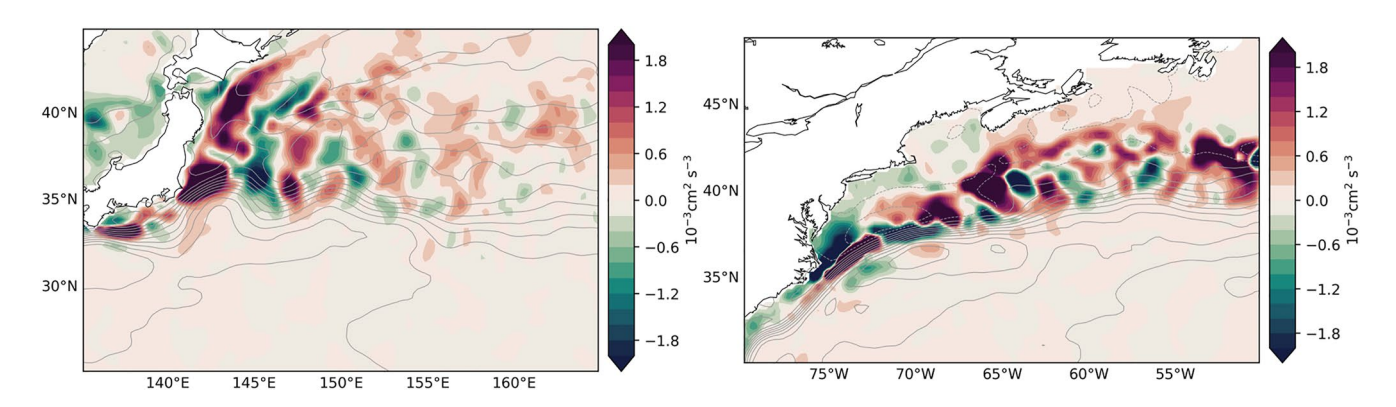


**Figure 12.** Rotational Baroclinic Conversion rate in the Kuroshio Extension (left) and Gulf Stream (right) based on satellite observations. Contour lines indicate sea surface height with CI = 0.2 m.

discrepancy is associated with higher eddy energy in the current climate models. Small et al. (2014) showed that the standard deviation of SST is strong in the CESM-H compared with the observations and that the ratio of that in the high-resolution simulation to the observations can reach a factor of two in the Kuroshio Extension, Gulf Stream, and Antarctic Circumpolar Current. The strong SST standard deviation represents the actual high variability in the model (Small et al., 2014). The larger SST variance in CESM-H is corresponding with stronger divergent EHF and its related energy conversions in the major currents is mentioned in Section 4.2.

It is noted in Figure 6 that unique spatial structures emerge in the  $Q_{div}^{V}$  with equatorward transport on the southern flanks of northern hemisphere western boundary currents. Two strong divergence patterns exist in the Kuroshio Extension in both the observations and model (Figures 6a and 6c). One is located south of Japan upstream of the Izu Ridge and the other is located near the separation at 35°N where the Kuroshio becomes a free jet. In the Gulf Stream (Figures 6b and 6d), large equatorward transport appears south of the jet path, which is strongest near the separation point off Cape Hatteras. These southward surface divergent EHFs observed in the Kuroshio Extension and Gulf Stream have a remarkable resemblance to the vertically integrated divergent transport computed from the OFES model (Aoki et al., 2013). In the Kuroshio Extension, the most prominent equatorward transport is centered at approximately 34.6°N, 142.4°E and in the Gulf Stream at 35.1°N, 73.1°W. These same features are observed at the thermocline depth in OFES at 33°N, 142.5°E and 34°N, 70.5°W in Aoki et al. (2013). Note that the core of equatorward transport at the thermocline depth is east of our surface estimate in the Gulf Stream. This eastward spatial shift with depth may be associated with the nonlinear temperature profile and vertical tilting of velocity (Tréguier et al., 2017). One possible mechanism for driving these nontrivial equatorward EHFs may be the advection of warm water by meanders and cold eddies that detach from jet as the secondary effect of baroclinic instability (Aoki et al., 2013).

Aoki et al. (2013) attempted to use the occurrence of high temperature water and skewness of temperature anomaly to interpret the equatorward flux. The occurrence of high temperature water is calculated by first determining temperature value (threshold) with minimum frequency based on temperature histogram, then counting the frequency of high temperature larger than the threshold. Adopted from their method, we show the high temperature water and skewness at 400 m using the ARMOR3D observational based data set (Figure 13). The high occurrence of warm water (>16°C in the Kuroshio Extension; >18°C in the Gulf Stream) and negative temperature skewness (indication to cold eddies and meander troughs) at the typical thermocline depth coincide with the surface equatorward divergent flux in both the Kuroshio Extension (Figures 13a and 13c) and Gulf Stream (Figures 13b and 13d). This observational-based result suggests that the existence of warm core water and advection from cold eddies (and meanders) contribute to the southward divergent EHFs in these regions in nature. Moreover, the strong connection of equatorward flux in the surface (Figure 13) and ocean interior (Aoki et al., 2013) also infers the possible footprint of thermocline instabilities at the ocean surface. Noted that these equatorward transports are not obvious in the Southern Hemisphere, where the mixed-layer divergent EHFs are mostly toward the South Pole with the exception of relatively weak northward transport at the southern tip of Africa (Figures 10a and 10b). Even though large equatorward transport of heat by mesoscale eddies appears in the above mentioned regions, its associated energy conversion (Figure 7) is weak, suggesting a trivial contribution of these equatorward fluxes on eddy-mean flow interactions.

GUO AND BISHOP 14 of 19

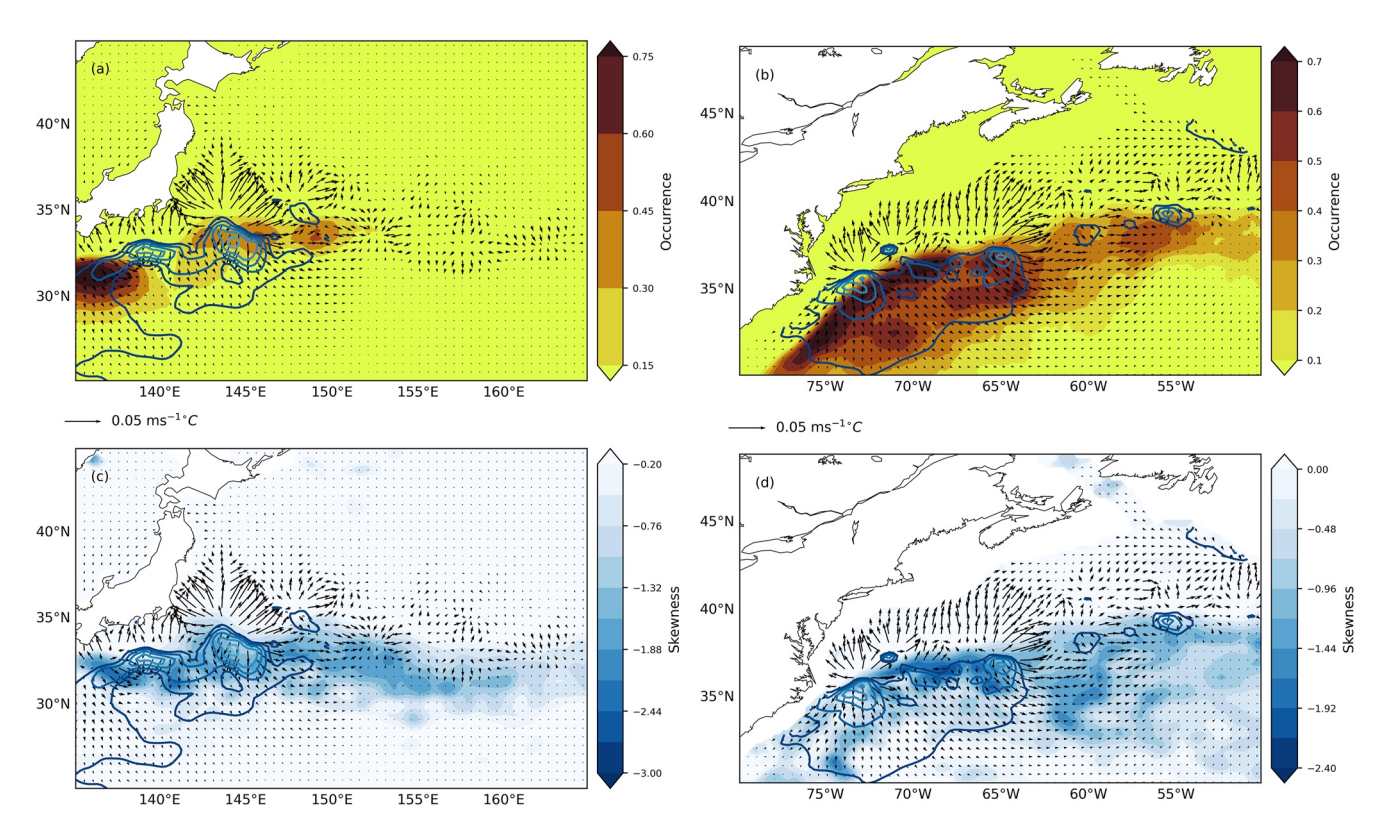


Figure 13. (a). Color denotes the frequency of high temperature water (>16°C) at 400 m and contour lines are the negative divergent eddy heat flux (EHF) in the Kuroshio Extension; (b). Color denotes the frequency of high temperature water (>18°C) at 400 m and contour lines are the negative divergent EHF in the Gulf Stream; (c). Color denotes the skewness of 400 m-temperature and contour lines represent negative divergent flux in the Kuroshio Extension; (d). Color denotes the skewness of 400 m-temperature and contour lines represent negative divergent flux in the Gulf Stream. Surface EHFs vectors are superimposed.

## 6. Conclusions

In this work, we reconstructed the surface global divergent EHFs as a proxy for the ocean mixed layer based on satellite observations and a high-resolution coupled CESM output. The global distribution of mixed-layer EHFs is well represented in CESM-H compared with observations. By solving a Poisson equation on the globe, we successfully decomposed the full EHF field into rotational and divergent components. The rotational flux generally circulates around the temperature variance and does not significantly contribute to the global energy budget. With the dynamically important divergent fluxes, we found that the majority of poleward meridional eddy heat transport in the mixed layer is concentrated near the midlatitudes, which is consistent with the results of previous model-based analysis (Aoki et al., 2013; Jayne & Marotzke, 2002). We further estimated the energy conversions from mean to EPE by computing the divergent flux-related baroclinic conversions. The BC<sub>div</sub> is shown to be mostly positive and its global surface area integration reaches an order of 0.1 TW. By smoothing the data spatially and temporally, it is found that 80% of the MPE-EPE conversion is confined to timescales less than 2 years and length scales less than 4°, within the mesoscale eddy band. We examined the model performance on simulating eddy-mean flow interactions through comparing surface EHFs and its related energy conversions with satellite observations. It is shown that CESM-H has relatively stronger divergent EHFs and larger BC rates that increased by a factor of 1-2 compared to the observations in northern hemisphere western boundary currents, while the model results are more consistent with observations in the Southern Hemisphere. A cross-spectrum analysis was performed to investigate the discrepancy, and we found that in regions of the Kuroshio Extension and Gulf Stream, the model has higher variance at the low-frequency bands (<1/10 month<sup>-1</sup>), while the model can capture the majority of dominant timescales found in the observations.

As one significant source of EPE generation in the ocean pathway, our surface estimate of BC (Figure 3c) has a remarkable similarity to the sink of EPE by mesoscale air-sea interaction (Bishop et al., 2020). Thus far the surface EPE conversion has been identified, but additional work is needed to compute full-depth BC and link it

GUO AND BISHOP 15 of 19



to the sink of EPE identified in Bishop et al. (2020) and other processes that can drive global EPE change (e.g., advection and interior dissipation). Further information on the full EPE budget in a high resolution ocean simulation will appear in Guo et al. (2022, submitted).

## Appendix A: Verification of Solutions to the Poisson Equation

The accuracy for solution to Equation 3 is verified in Figure A1 with plots of source term derived from the solution to the Poisson equation  $\nabla^2 \phi$ , original source term from EHF field  $\nabla \cdot \vec{u}'\theta'$ , difference between reconstructed and input source terms, and zonal integrals of the abovementioned three maps. It is shown that the error is very small, and there is only a slight difference between the reconstructed and original source terms based on their zonal integrals (Figure A1).

We further examined the sensitivity of different boundary conditions to the solution. The  $Q_y^{div}$  computed with different boundary conditions are demonstrated in Figures A2a and A2b, which were solved with the Neumann boundary and Dirichlet boundary on coarsened 1-degree global grid. A slight difference between the two solutions is observed from their zonal integrations. Overall, no significant discrepancy is found in terms of geographic distributions and magnitudes.

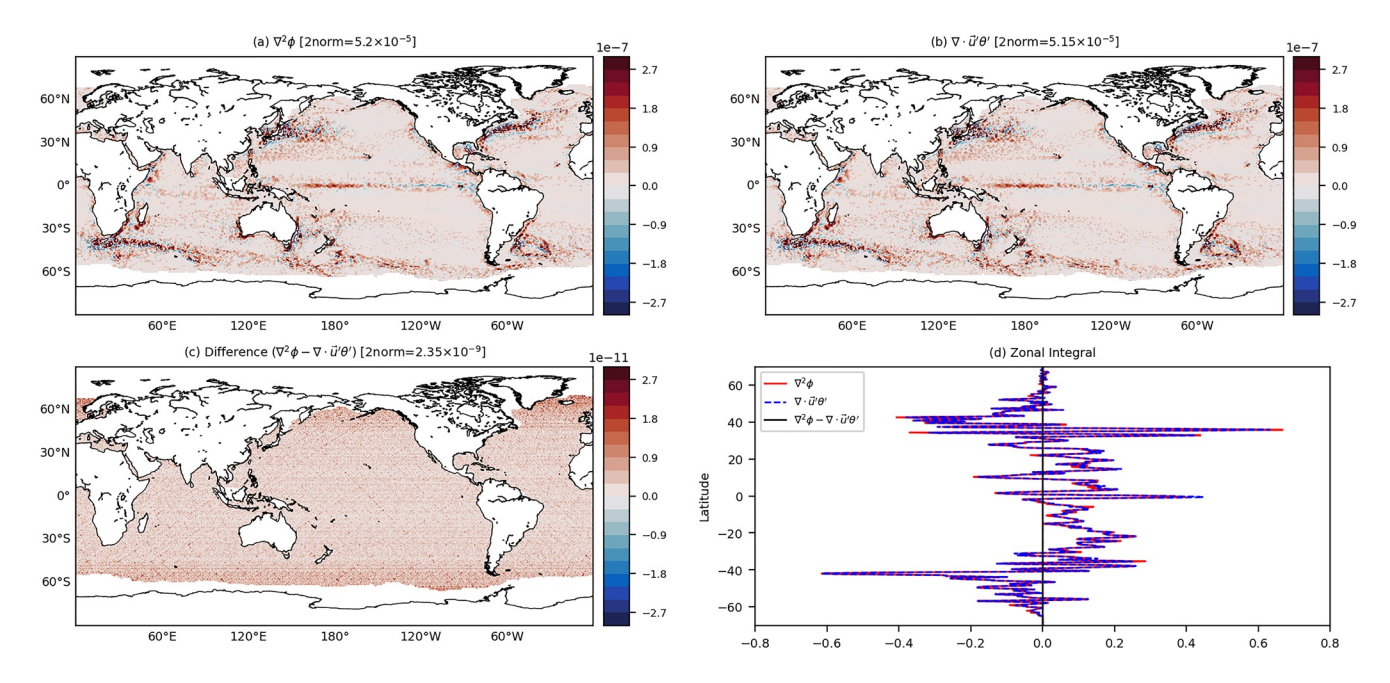


**Figure A1.** Top left: Source term  $(\nabla^2 \phi)$  from solution Equation 3; Top right: Original source term  $(\nabla \cdot \vec{u'}\theta')$  directly calculated from data; Bottom left: Error map between reconstructed source term and original source term  $(\nabla^2 \phi - \nabla \cdot \vec{u'}\theta')$ ; Bottom right: corresponding zonal integrals.

GUO AND BISHOP 16 of 19

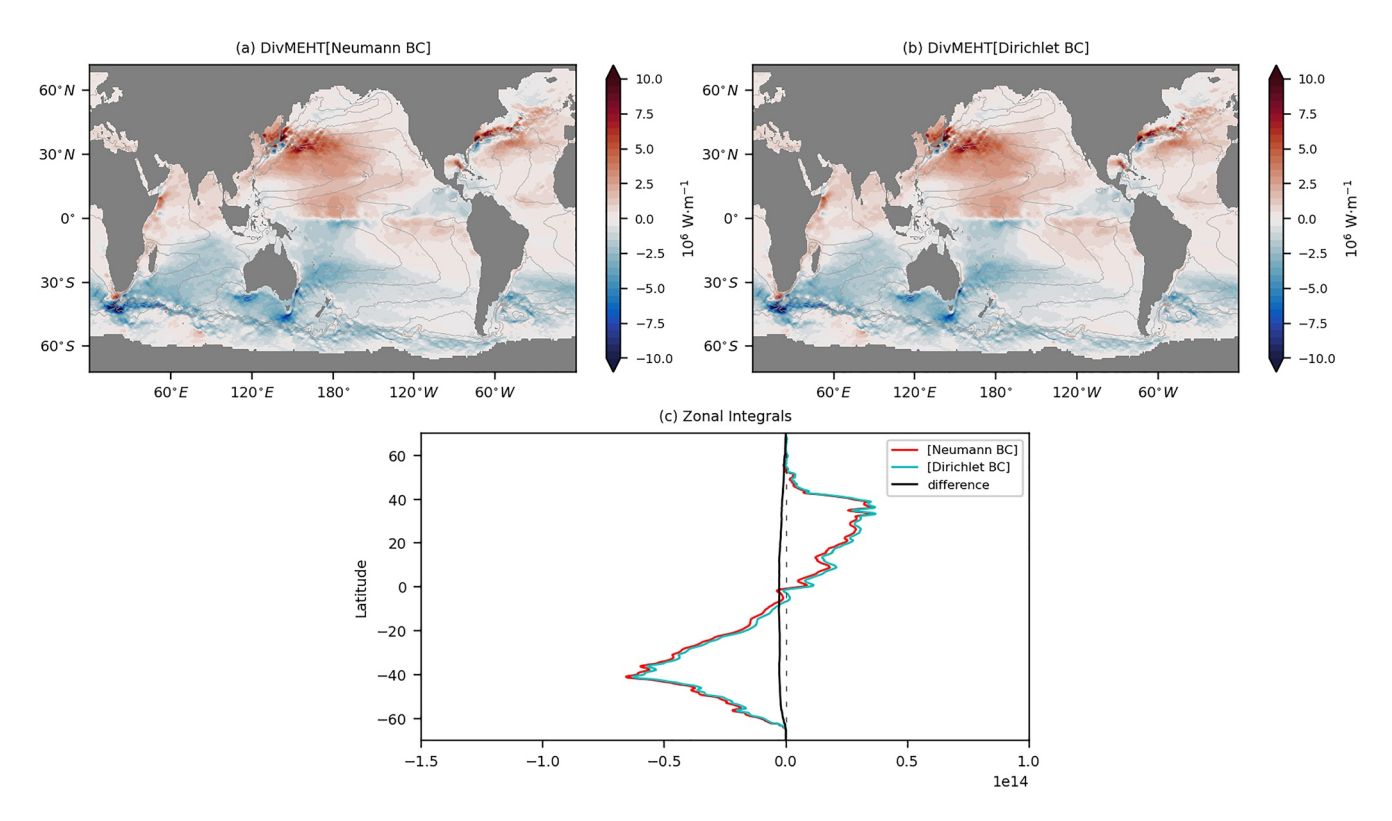


Figure A2. Divergent eddy heat transport in the mixed layer based on satellite observations extracted by solving Equation 3 with Neumann boundary condition (top left) and Dirichlet boundary condition (top right); Mean sea surface height contours are indicated by gray contours (CI = 0.2 m). Zonal integrals of the two solutions and their difference are given on the bottom.

## **Data Availability Statement**

All data used in this paper can be freely downloaded online. Sea surface height, surface geostrophic velocity, and ARMOR3D data can be found at <a href="http://marine.copernicus.eu">http://marine.copernicus.eu</a>; NOAA high resolution sea surface temperature data is provided by the NOAA/OAR/ESRL PSL, Boulder, Colorado, USA, from their web site at <a href="https://psl.noaa.gov/">https://psl.noaa.gov/</a>; Monthly Isopycnal & Mixed-layer Ocean Climatology data set is available at <a href="https://www.pmel.noaa.gov/mimoc/">https://www.pmel.noaa.gov/mimoc/</a>; The CESM-H data set is available at the Earth System Grid on <a href="https://www.earthsystemgrid.org/">https://www.earthsystemgrid.org/</a>.

#### Acknowledgments

This work was supported by the National Science Foundation through the Award 2023590. We thank the US CLIVAR workshop on the Sources and Sinks of Mesoscale Eddy Energy held in Tallahassee, Florida on March, 2019. This work was greatly improved by discussions during the workshop. We thank Stephen Griffies, Annalisa Bracco, and two anonymous reviewers for their help in improving this manuscript.

#### References

Abernathey, R., & Cessi, P. (2014). Topographic enhancement of eddy efficiency in baroclinic equilibration. *Journal of Physical Oceanography*, 44(8), 2107–2126. https://doi.org/10.1175/jpo-d-14-0014.1

Abernathey, R., & Wortham, C. (2015). Phase speed cross spectra of eddy heat fluxes in the eastern Pacific. *Journal of Physical Oceanography*, 45(5), 1285–1301. https://doi.org/10.1175/jpo-d-14-0160.1

Aoki, K., Minobe, S., Tanimoto, Y., & Sasai, Y. (2013). Southward eddy heat transport occurring along southern flanks of the Kuroshio Extension and the Gulf Stream in a 1/10° global ocean general circulation model. *Journal of Physical Oceanography*, 43(9), 1899–1910. https://doi.org/10.1175/jpo-d-12-0223.1

Bishop, S. P. (2013). Divergent eddy heat fluxes in the Kuroshio Extension at 144–148°E. Part II: Spatiotemporal variability. *Journal of Physical Oceanography*, 43(11), 2416–2431. https://doi.org/10.1175/jpo-d-13-061.1

Bishop, S. P., Bryan, F. O., & Small, R. J. (2015). Bjerknes-like compensation in the wintertime North Pacific. *Journal of Physical Oceanogra*phy, 45(5), 1339–1355. https://doi.org/10.1175/jpo-d-14-0157.1

Bishop, S. P., Gent, P. R., Bryan, F. O., Thompson, A. F., Long, M. C., & Abernathey, R. (2016). Southern Ocean overturning compensation in an eddy-resolving climate simulation. *Journal of Physical Oceanography*, 46(5), 1575–1592. https://doi.org/10.1175/jpo-d-15-0177.1

Bishop, S. P., Small, R. J., & Bryan, F. O. (2020). The global sink of available potential energy by mesoscale Air-sea interaction. *Journal of Advances in Modeling Earth Systems*, 12(10), e2020MS002118. https://doi.org/10.1029/2020ms002118

Bishop, S. P., Small, R. J., Bryan, F. O., & Tomas, R. A. (2017). Scale dependence of midlatitude air–sea interaction. *Journal of Climate*, 30(20), 8207–8221. https://doi.org/10.1175/jcli-d-17-0159.1

Bishop, S. P., Watts, D. R., & Donohue, K. A. (2013). Divergent eddy heat fluxes in the Kuroshio Extension at 144–148°E. Part I: Mean structure. Journal of Physical Oceanography, 43(8), 1533–1550. https://doi.org/10.1175/jpo-d-12-0221.1

Bryden, H. L., & Heath, R. A. (1985). Energetic eddies at the northern edge of the Antarctic Circumpolar Current in the southwest Pacific. *Progress in Oceanography*, 14, 65–87. https://doi.org/10.1016/0079-6611(85)90006-0

GUO AND BISHOP 17 of 19



- Chelton, D. B., Gaube, P., Schlax, M. G., Early, J. J., & Samelson, R. M. (2011). The influence of nonlinear mesoscale eddies on near-surface oceanic chlorophyll. Science, 334(6054), 328–332. https://doi.org/10.1126/science.1208897
- Chelton, D. B., Schlax, M. G., & Samelson, R. M. (2011). Global observations of nonlinear mesoscale eddies. *Progress in Oceanography*, 91(2), 167–216. https://doi.org/10.1016/j.pocean.2011.01.002
- Chi, L., Wolfe, C. L., & Hameed, S. (2018). Intercomparison of the Gulf stream in ocean reanalyses: 1993–2010. Ocean Modelling, 125, 1–21. https://doi.org/10.1016/j.ocemod.2018.02.008
- Cronin, M., & Watts, D. R. (1996). Eddy-mean flow interaction in the Gulf Stream at 68°W. Part I: Eddy energetics. *Journal of Physical Ocean-ography*, 26(10), 2107–2131. https://doi.org/10.1175/1520-0485(1996)026<2107:efiitg>2.0.co;2
- Cronin, M. F., Bond, N. A., Farrar, J. T., Ichikawa, H., Jayne, S. R., Kawai, Y., et al. (2013). Formation and erosion of the seasonal thermocline in the Kuroshio Extension Recirculation Gyre. Deep Sea Research Part II: Topical Studies in Oceanography, 85, 62–74. https://doi.org/10.1016/j. dsr2.2012.07.018
- Dewar, W. K., & Bane, J. M. (1989). Gulf stream dynamics. Pad II: Eddy energetics at 73°W. Journal of Physical Oceanography, 19(10), 1574–1587. https://doi.org/10.1175/1520-0485(1989)019<1574;gsdpie>2.0.co;2
- Dong, C., McWilliams, J. C., Liu, Y., & Chen, D. (2014). Global heat and salt transports by eddy movement. *Nature Communications*, 5, 3294. https://doi.org/10.1038/ncomms4294
- Eden, C., Greatbatch, R. J., & Olbers, D. (2007). Interpreting eddy fluxes. Journal of Physical Oceanography, 37(5), 1282–1296. https://doi.org/10.1175/jpo3050.1
- Ferrari, R., Provost, C., Park, Y.-H., Sennéchael, N., Koenig, Z., Sekma, H., et al. (2014). Heat fluxes across the Antarctic circumpolar current in Drake passage: Mean flow and eddy contributions. *Journal of Geophysical Research: Oceans*, 119(9), 6381–6402. https://doi. org/10.1002/2014jc010201
- Foppert, A., Donohue, K. A., Watts, D. R., & Tracey, K. L. (2017). Eddy heat flux across the Antarctic Circumpolar Current estimated from sea surface height standard deviation. *Journal of Geophysical Research: Oceans*, 122(8), 6947–6964. https://doi.org/10.1002/2017jc012837
- Fox-Kemper, B., Ferrari, R., & Pedlosky, J. (2003). On the indeterminacy of rotational and divergent eddy fluxes. *Journal of Physical Oceanog-raphy*, 33(2), 478–483. https://doi.org/10.1175/1520-0485(2003)033<0478:otiora>2.0.co;2
- Gent, P. R., & Mcwilliams, J. C. (1990). Isopycnal mixing in ocean circulation models. *Journal of Physical Oceanography*, 20(1), 150–155. https://doi.org/10.1175/1520-0485(1990)020<0150:imiocm>2.0.co;2
- Greatbatch, R. J., Zhai, X., Eden, C., & Olbers, D. (2007). The possible role in the ocean heat budget of eddy-induced mixing due to air-sea interaction. *Geophysical Research Letters*, 34(7), L07604. https://doi.org/10.1029/2007gl029533
- Guinehut, S., Dhomps, A.-L., Larnicol, G., & Le Traon, P.-Y. (2012). High resolution 3-D temperature and salinity fields derived from in situ and satellite observations. *Ocean Science*, 8(5), 845–857. https://doi.org/10.5194/os-8-845-2012
- Guo, Y., Bishop, S., Bryan, F., & Bachman, S. (2022). A global diagnosis of eddy potential energy budget in an eddy permitting ocean model. *Journal of Physical Oceanography*. (submitted).
- Hall, M. M. (1986). Assessing the energetics and dynamics of the Gulf Stream at 68W from moored current measurements. *Journal of Marine Research*, 44(3), 423–443. https://doi.org/10.1357/002224086788403033
- Hunke, E. C., Lipscomb, W. H., Turner, A. K., Jeffery, N., & Elliott, S. (2010). CICE: The Los Alamos sea ice model documentation and software user's manual version 4.1 LA-CC-06-012. T-3 Fluid Dynamics Group Los Alamos National Laboratory, 675, 500.
- Hurrell, J. W., Holland, M. M., Gent, P. R., Ghan, S., Kay, J. E., Kushner, P. J., et al. (2013). The Community Earth System Model: A framework for collaborative research. Bulletin of the American Meteorological Society, 94(9), 1339–1360. https://doi.org/10.1175/bams-d-12-00121.1
- Jayne, S. R., & Marotzke, J. (2002). The oceanic eddy heat transport. *Journal of Physical Oceanography*, 32(12), 3328–3345. https://doi.org/10.1175/1520-0485(2002)032<3328:toeht>2.0.co;2
- Killworth, P. D. (1992). An equivalent-barotropic mode in the Fine Resolution Antarctic Model. *Journal of Physical Oceanography*, 22(11), 1379–1387. https://doi.org/10.1175/1520-0485(1992)022<1379;aebmit>2.0.co;2
- Lagerloef, G. S., Mitchum, G. T., Lukas, R. B., & Niiler, P. P. (1999). Tropical Pacific near-surface currents estimated from altimeter, wind, and drifter data. *Journal of Geophysical Research*, 104(C10), 23313–23326. https://doi.org/10.1029/1999jc900197
- Lau, N.-C., & Wallace, J. M. (1979). On the distribution of horizontal transports by transient eddies in the northern hemisphere wintertime circulation. *Journal of the Atmospheric Sciences*, 36(10), 1844–1861. https://doi.org/10.1175/1520-0469(1979)036<1844:otdoht>2.0.co;2
- Lawrence, D. M., Oleson, K. W., Flanner, M. G., Thornton, P. E., Swenson, S. C., Lawrence, P. J., et al. (2011). Parameterization improvements and functional and structural advances in version 4 of the Community Land Model. *Journal of Advances in Modeling Earth Systems*, 3(1), M03001, https://doi.org/10.1029/2011ms00045
- Ma, X., Jing, Z., Chang, P., Liu, X., Montuoro, R., Small, R. J., et al. (2016). Western boundary currents regulated by interaction between ocean eddies and the atmosphere. *Nature*, 535(7613), 533–537, https://doi.org/10.1038/nature18640
- Marshall, J., & Shutts, G. (1981). A note on rotational and divergent eddy fluxes. *Journal of Physical Oceanography*, 11(12), 1677–1680. https://doi.org/10.1175/1520-0485(1981)011<1677;anorad>2.0.co;2
- McClean, J. L., Bader, D. C., Bryan, F. O., Maltrud, M. E., Dennis, J. M., Mirin, A. A., et al. (2011). A prototype two-decade fully-coupled fine-resolution CCSM simulation. *Ocean Modelling*, 39(1–2), 10–30. https://doi.org/10.1016/j.ocemod.2011.02.011
- McWilliams, J. C., Gula, J., Molemaker, M. J., Renault, L., & Shchepetkin, A. F. (2015). Filament frontogenesis by boundary layer turbulence. Journal of Physical Oceanography, 45(8), 1988–2005. https://doi.org/10.1175/jpo-d-14-0211.1
- Mulet, S., Rio, M.-H., Mignot, A., Guinehut, S., & Morrow, R. (2012). A new estimate of the global 3D geostrophic ocean circulation based on satellite data and in-situ measurements. *Deep Sea Research Part II: Topical Studies in Oceanography*, 77, 70–81. https://doi.org/10.1016/j.
- Park, S., Bretherton, C. S., & Rasch, P. J. (2014). Integrating cloud processes in the Community Atmosphere Model, version 5. Journal of Climate, 27(18), 6821–6856. https://doi.org/10.1175/jcli-d-14-00087.1
- Phillips, H. E., & Rintoul, S. R. (2000). Eddy variability and energetics from direct current measurements in the Antarctic Circumpolar Current south of Australia. *Journal of Physical Oceanography*, 30(12), 3050–3076. https://doi.org/10.1175/1520-0485(2000)030<3050:evaefd>2.0.co;2
- Reynolds, R. W., Smith, T. M., Liu, C., Chelton, D. B., Casey, K. S., & Schlax, M. G. (2007). Daily high-resolution-blended analyses for sea surface temperature. *Journal of Climate*, 20(22), 5473–5496. https://doi.org/10.1175/2007jcli1824.1
- Schmidtko, S., Johnson, G. C., & Lyman, J. M. (2013). MIMOC: A global monthly isopycnal upper-Ocean Climatology with mixed layers. *Journal of Geophysical Research: Oceans*, 118(4), 1658–1672. https://doi.org/10.1002/jgrc.20122
- Small, R. J., Bacmeister, J., Bailey, D., Baker, A., Bishop, S., Bryan, F., et al. (2014). A new synoptic scale resolving global climate simulation using the Community Earth System Model. *Journal of Advances in Modeling Earth Systems*, 6(4), 1065–1094. https://doi.org/10.1002/2014ms000363
- Small, R. J., Bryan, F. O., Bishop, S. P., & Tomas, R. A. (2019). Air–sea turbulent heat fluxes in climate models and observational analyses: What drives their variability? *Journal of Climate*, 32(8), 2397–2421. https://doi.org/10.1175/jcli-d-18-0576.1

GUO AND BISHOP 18 of 19



- Smith, R., Jones, P., Briegleb, B., Bryan, F., Danabasoglu, G., Dennis, J., et al. (2010). The parallel ocean program (POP) reference manual: Ocean component of the community climate system model (CCSM) and Community Earth System Model (CESM). *LAUR-01853*, *141*, 1–140. Stammer, D. (1998). On eddy characteristics, eddy transports, and mean flow properties. *Journal of Physical Oceanography*, *28*(4), 727–739. https://doi.org/10.1175/1520-0485(1998)028<0727:oeceta>2.0.co;2
- Tréguier, A.-M., Lique, C., Deshayes, J., & Molines, J.-M. (2017). The North Atlantic eddy heat transport and its relation with the vertical tilting of the Gulf Stream axis. *Journal of Physical Oceanography*, 47(6), 1281–1289. https://doi.org/10.1175/jpo-d-16-0172.1
- Verbrugge, N., Mulet, S., Guinehut, S., & Buongiorno-Nardelli, B. (2017). ARMOR3D: A 3D multi-observations T, S, U, V product of the ocean. EGU general assembly conference abstracts, 19, 17579.
- Volkov, D. L., Lee, T., & Fu, L.-L. (2008). Eddy-induced meridional heat transport in the ocean. *Geophysical Research Letters*, 35(20), L20601. https://doi.org/10.1029/2008g1035490
- Von Storch, J.-S., Eden, C., Fast, I., Haak, H., Hernández-Deckers, D., Maier-Reimer, E., et al. (2012). An estimate of the Lorenz energy cycle for the world ocean based on the STORM/NCEP simulation. *Journal of Physical Oceanography*, 42(12), 2185–2205. https://doi.org/10.1175/jpo-d-12-079.1
- Watts, D. R., Tracey, K. L., Donohue, K. A., & Chereskin, T. K. (2016). Estimates of eddy heat flux crossing the Antarctic Circumpolar Current from observations in Drake Passage. *Journal of Physical Oceanography*, 46(7), 2103–2122. https://doi.org/10.1175/jpo-d-16-0029.1
- Wenegrat, J. O., Thomas, L. N., Gula, J., & McWilliams, J. C. (2018). Effects of the submesoscale on the potential vorticity budget of ocean mode waters. *Journal of Physical Oceanography*, 48(9), 2141–2165. https://doi.org/10.1175/jpo-d-17-0219.1
- Zhai, X., & Greatbatch, R. J. (2006). Inferring the eddy-induced diffusivity for heat in the surface mixed layer using satellite data. *Geophysical Research Letters*, 33(24), L24607. https://doi.org/10.1029/2006gl027875

GUO AND BISHOP 19 of 19